T2R2 東京科学大学 リサーチリポジトリ
Science Tokyo Research Repository

論文 / 著書情報
Article / Book Information

題目(和文)	非平衡プラズマにおける振動励起CO2の触媒表面反応に関する反応機構の研究
Title(English)	Mechanistic study on the catalytic surface reaction of vibrationally-excited CO2 in nonthermal plasma
著者(和文)	KIM DAE-YEONG
Author(English)	KIM DAE-YEONG
出典(和文)	学位:博士(工学), 学位授与機関:東京工業大学, 報告番号:甲第12359号, 授与年月日:2023年3月26日, 学位の種別:課程博士, 審査員:野崎 智洋,関口 秀俊,山中 一郎,山本 貴富喜,笹部 崇
Citation(English)	Degree:Doctor (Engineering), Conferring organization: Tokyo Institute of Technology, Report number:甲第12359号, Conferred date:2023/3/26, Degree Type:Course doctor, Examiner:,,,,
学位種別(和文)	博士論文
Type(English)	Doctoral Thesis

Powered by T2R2 (Science Tokyo Research Repository)

Mechanistic study on the catalytic surface reaction of vibrationally-excited CO_2 in nonthermal plasma

A THESIS
SUBMITTED TO THE FACILITY OF SCHOOL OF ENGINEERING,
GRADUATE MAJOR OF MECHANICAL ENGINEERING
OF TOKYO INSTITUTE OF TECHNOLOGY
BY

DAE-YEONG KIM

IN PARTIAL FULFILLMENT OF THE REQUIREMENTS
FOR THE DEGREE OF
DOCTOR OF ENGINEERING

SUPERVISOR:
PROFESSOR TOMOHIRO NOZAKI

FEBRUARY 2023

Abstract

Nonthermal plasma (NTP) assisted catalysis is gaining attention as an attractive technology that can overcome the energy barriers involved in conventional thermal catalysis. However, the catalytic surface reaction dynamics of NTP-activated species are still primitive. Generally, interactions between catalytic surface and gas molecules follow three well-established mechanisms: Langmuir-Hinshelwood, Eley−Rideal, and Mars−van Krevelen type mechanisms. In this thesis, I present the elucidation of the microscopic mechanism of NTP-assisted catalysis. In particular, I focus on the interaction between vibrationally-excited molecules and the catalyst surface. First, I explore the CO_2 hydrogenation over Pd_2Ga/SiO_2 alloy catalysts via the Eley−Rideal type mechanism. Then, I investigate the CO oxidation over wurtzite ZnO via the Mars−van Krevelen type mechanism.

Table of content

List of figures

spectra of surface species on Pd_2Ga/SiO_2. A CO_2 + H_2 mixture was introduced at a constant flow rate, while reaction conditions were switching from thermal to DBD to thermal for every 8 min.

Figure 2.14. Identification of the influence of gas phase CO_2 dissociation to CO under DBD conditions with QMS. QMS signal over the (a) Blank, (b) SiO_2 and (c) Pd_2Ga/SiO_2 at 250 °C under CO_2 (10 mL min^{-1}) + H_2 (30 mL min^{-1}) diluted in Ar (150 mL min^{-1}). DBD was turned on from 8 min to 12 min, comparing thermal and DBD hybrid reactions. To clarify the influence of the DBD-induced gas phase reaction, under the thermal and DBD transient experiments over the without catalyst (Blank), SiO_2, and Pd_2Ga/SiO_2 with CO_2 + H_2 mixture QMS studies were performed. Under these conditions, the plasma power was 0.1 W. Upon turning on DBD, a CO signal was not detected by QMS with Blank experiment. In the case of SiO_2, compared to the Blank experiment, a faint CO signal was observed by QMS, indicating that CO_2 dissociation to CO by DBD is not promoted. In contrast, in the case of Pd_2Ga/SiO_2, a CO signal increased clearly during DBD treatment. Generation of CO originates DBD-induced catalyst reaction and gas phase CO_2 dissociation to CO by DBD is negligible.

Figure 2.15. Identification of the reaction intermediates for CO_2 hydrogenation over Pd_2Ga/SiO_2. (a,b) *In situ* TIR spectra where the feed gas was switched alternately between H_2 and CO_2 for 6 min interval under the DBD (a) and thermal (b) conditions. (c) *In situ* TIR spectra where the feed gas was switched alternately between CO_2 + H_2 mixture and CO_2 for 6 min interval. (d) Relative intensities attributed to CO_L (2077 cm^{-1}), m-HCOO (1368 cm^{-1}), and b-HCOO (1355 cm^{-1}) in (c) as a function of time.

Figure 2.16. *In situ* TIR spectra over SiO_2 where the feed gas was switched alternately between H_2 and CO_2 for 6 min interval under the DBD conditions.

Figure 2.17. Walsh diagram of CO_2 orbital energies in linear and bent geometries. Based on the

linear geometry (180°), the schematics of the molecular orbitals are shown on the left side, and the symmetry properties of the orbital are shown on the right side. The molecular orbital most relevant to reactivity are the $1\pi_g$ and $2\pi_u$ orbitals roles as the highest occupied molecular orbital (HOMO) and the lowest unoccupied molecular orbital (LUMO), respectively. According to Walsh's rule, CO_2 adopts a linear shape. On the other hand, due to environmental factors, when LUMO is filled with electrons, the energy of the bent shape of CO_2 is more stabilized than linear shape. Also, the bending mode of vibrationally-excited CO_2 by plasma can induce changes in the shape and energy level of LUMO.

Figure 2.18. *In situ* XAFS results of the Pd_2Ga/SiO_2 during CO_2 hydrogenation with and without DBD. (a) Ga and (c) Pd K-edge XANES. (b) Ga and (d) Pd K-edge k^3-weighted EXAFS oscillation, Fourier−transformed (FT) EXAFS and inversely FT EXAFS data are shown with the black fitted curves (see Tables 2.3 and 2.4 for the details of the fitting). k-range for FT: 3.0−15.0 $Å^{-1}$; Ar = 100 mL min^{-1}; H_2 = 30 mL min^{-1}; CO_2 = 10 mL min^{-1}; pressure = 10 kPa; Reaction temperature = 250 ºC.

Figure 2.19. DFT calculations of the CO_2 hydrogenation reactions on $Pd_2Ga(020)$. (a) Energy diagram. (b) Corresponding DFT optimized geometries, showing the energy barriers. Color scheme: black, palladium; green, gallium; gray, carbon; red, oxygen; and white, hydrogen.

Figure 2.20. Proposed reaction mechanism of the CO_2 hydrogenation. Schematic illustration showing the CO_2 hydrogenation over the Pd_2Ga/SiO_2 by the vibrationally-excited CO_2 under NTP conditions via the E−R pathway.

Figure 3.1. (XRD patterns of ZnO. The inset shows the SEM image of ZnO, indicating it is hexagonal.

Figure 3.2. (a) 3D Schematic illustration of *in situ* TIR DBD reactor which is capable of identifying catalytic surface species with and without DBD irradiation. Gas-phase IR

absorption spectroscopy is also possible using blank TIR reactor (without catalyst pellet). (b) 3D schematic diagram electrodes and ZnO pellet geometry. (c) Photograph emission from DBD (0.058W).

Figure 3.3. (a) Vibrationally-excited CO TIR spectra taken at DBD power of 0.058 W at 2 % CO in Ar (50 cm^3 min^{-1}) stream at room temperature. (b) Comparison between simulated and experimental CO TIR spectra at same conditions with (a). (c) Rotational and vibrational temperatures measured at DBD power of 0.058, 0.066, and 0.078 W at 2 % CO in Ar stream.

Figure 3.4. Density distribution of vibrationally-excited CO calculated at vibrational temperatures of 1000, 1100 and 1300 K while gas temperature is assumed to be constant at 300 K. Y-axis represents mol % of density of vibrationally-excited CO relative to total CO density.

Figure 3.5. *In situ* TIR spectra of (a) (bi)carbonates and (b,c) CO-related region over ZnO under thermal and DBD (0.058 W). ZnO was exposed to 2 % CO in Ar (50 cm^3 min^{-1}) stream at 300 K for 20 min.

Figure 3.6. *In situ* TIR spectra over ZnO under thermal DBD (0.058 W). The ZnO was pretreated the at 770 K in Ar atmosphere for 1 h, and thereafter exposed to 2 % CO in Ar (50 cm^3 min^{-1}) stream at 470 K for 20 min.

Figure 3.7. *In situ* TIR spectra OH groups region over ZnO under DBD conditions corresponding Figure 3.6 (yellow) and Figure 3.7 (purple).

Figure 3.8. (a) *In situ* TIR spectra of CO-related region at different DBD power after 5 min and (b) corresponding evolution of carbonate (1514 cm^{-1}). ZnO was exposed to 2 % CO in Ar (50 cm^3 min^{-1}) stream at 300 K for 20 min with DBD power of 0.058, 0.066, and 0.078 W.

Figure 3.9. *In situ* TIR spectra over ZnO of (bi)carbonate-related region at different DBD power.

Figure 3.10. Schematic illustration of the promoting CO oxidation via Mars−van Krevelen type

mechanism by vibrationally-excited CO over ZnO. V_o: oxygen vacancies, O_L: lattice oxygen. I. Generation of vibrationally-excited CO by electron impact. II. Adsorption of vibrationally-excited CO to Zn^{2+}. III. (Bi)Carbonate formation by reaction with adsorbed CO and adjacent lattice oxygen.

List of tables

Chapter 1. Introduction

1.1 Motivation and outline

Nonthermal plasma (NTP) assisted catalysis is gaining increasing attention as emerging technologies can improve existing technologies in various applications, such as CO_2 hydrogenation[1,2], CH_4 dry reforming[3,4], ammonia synthesis[5-7], and more (Figure 1.1). As summarized in various NTP-assisted catalysis review papers[8-15], the advantages of NTP-assisted catalysis over thermal catalysis are achieved by combining the high selectivity of the catalyst with the high reactivity of the NTP. NTP is characterized by having abundant vibrationally-excited molecules with various active species including ions, radicals, and free electrons which arise due to inelastic collisions between high-energy electrons and ground-state molecules[9,14,16]. This effectively makes thermodynamically challenging reactions possible by removing the thermal equilibrium limitations experienced in thermal catalysis. Moreover, the NTP process offers the advantage of integrating with renewable energy with high variabilities of energy production, such as solar and wind power, as it operates instantaneously and provides the flexibility to be turned on/off quickly as needed[12,13,17]. Therefore, the purpose of NTP-assisted catalysis is to synthesize the desired product with high selectivity and energy efficiency as well as high conversion of reactants by generating active species from NTP and reacting them on the catalyst surface.

Although the synergistic effects in NTP-assisted catalysis are elicited by the rational design of catalysts, they depend on an understanding of the surface activity and reaction mechanisms relationships at the molecular level. A search for the topic “Plasma catalysis” on the Web of Science provides 4279 papers from the last 10 years. Although a significant number of studies on NTP-assisted catalysis have shown synergistic effects of combining NTP and catalysis, However, Due to the complex interaction between the plasma discharge and the catalyst in NTP-assisted catalysis, the explanation of the fundamental mechanism has yet to be established.

Catalytic surface chemistry is an important factor in NTP-assisted catalysis. The nature of the various reactions occurring on the catalytic surface determines the activity of the entire process of NTP-assisted catalysis[11]. The interactions at the catalytic surface of gas molecules (reactants) generally follow three well-established mechanisms: Langmuir–Hinshelwood (L–H); Two reactants adsorbed on catalyst surface react with each other, Eley–Rideal (E–R); Gas-phase reactants directly react with reactant previously adsorbed on catalyst surfaces, and Mars–van Krevelen (MvK) mechanisms; Reactants react with lattice components of catalysts, and spent components are recovered through second reactant (Figure 1.2). In the NTP conditions, vibrationally-excited molecules are dominant channels because of their low energy threshold compared with ionization or dissociation[4,7,13]. Accordingly, I believed that elucidating the interplay between vibrationally-excited molecules and catalytic surfaces is a great step forward for the clear-cut understanding of the synergistic effect and a prerequisite for the rational catalytic design for NTP-assisted catalysis.

In **Chapter 2**, I explored the reaction promotion of NTP-assisted catalysis by vibrationally-excited CO_2 via the E–R type mechanism. I focused on the CO_2 hydrogenation over Pd_2Ga/SiO_2 intermetallic catalysts. Although both thermal and NTP conditions showed close to 100% CO selectivity, it is worth emphasizing that when activated by NTP, CO_2 conversion not only improves more than 2-fold under thermal conditions but also breaks the thermodynamic equilibrium limitation. Mechanistic insight into NTP-activated species and intermetallic catalyst surface were investigated by using *in situ* transmission infrared (TIR) spectroscopy, where catalyst surface species were identified during NTP irradiation. Moreover, in *in situ* X-ray absorption fine-structure analysis under reaction conditions, the catalyst under NTP conditions not only did not undergo restructuring affecting CO_2 hydrogenation but also could clearly rule out catalyst activation by heating. *In situ* characterizations of the catalysts during CO_2 hydrogenation depict that vibrationally-excited CO_2 significantly enhances the catalytic reaction. the agreement of approaches combining experimental studies and density functional theory (DFT) calculations substantiates that vibrationally-excited CO_2 reacts directly with hydrogen adsorbed on Pd sites (via E−R type mechanism) while accelerating formate formation due to neighboring Ga sites. Moreover, DFT analysis deduces the key reaction pathway that the decomposition of monodentate formate is promoted by plasma-activated hydrogen species. I believed that the understanding and insights in **Chapter 2** enable the high designability of CO_2 hydrogenation catalysts toward value-added chemicals based on the electrification of chemical processes via NTP.

In **Chapter 3**, I focused on the reaction promotion of NTP-assisted catalysis by vibrationally-excited CO via the MvK mechanism. First, I was able to unambiguously identify vibrationally-excited CO species with *in situ* TIR diagnostics performed in a catalyst-free environment. The rotational temperature of CO remained unchanged at room temperature (ca. 300 K) at various NTP powers, while the vibrational temperature was increased from 1000 K to 1300 K with NTP power, showing that CO is excited into the vibrational quantum number of three. Then, the effect of NTP, or vibrationally-excited CO, was studied using surface reaction over wurtzite ZnO. A comparative study with ground-state CO by *in situ* TIR spectroscopy suggests that vibrationally-excited CO over the wurtzite ZnO surface promotes thermodynamically limited CO oxidation at room temperature. The spectral evidence shows that vibrationally-excited CO exhibits an unusual CO adsorption band due to strong binding energy with Zn^{2+}, which improves the CO oxidation by activating the reaction with adjacent lattice oxygen in the wurtzite ZnO via the Mar−van Krevelen type mechanism at room temperature. The present findings provide new possibilities for achieving low temperature CO oxidation based on the electrification of chemical processes through NTP.

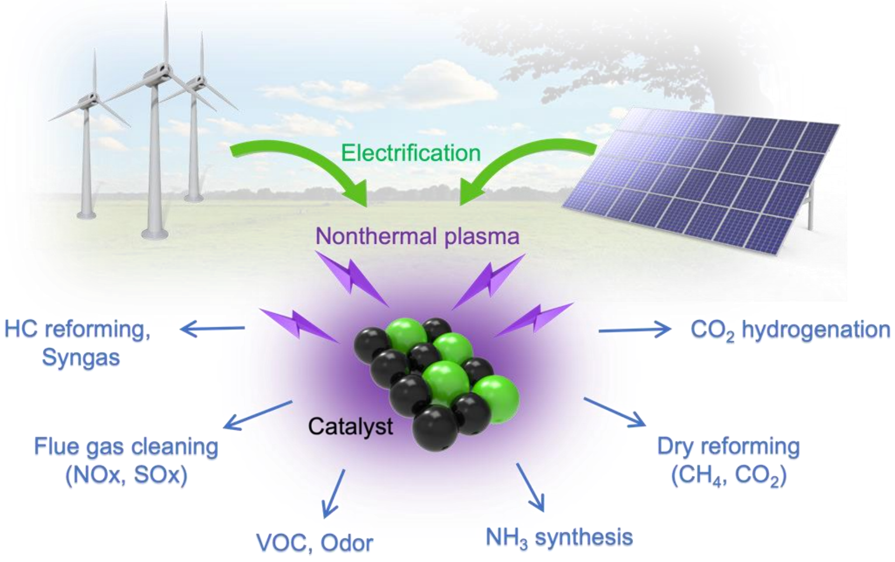

Figure 1.1. Application of NTP-assisted catalysis

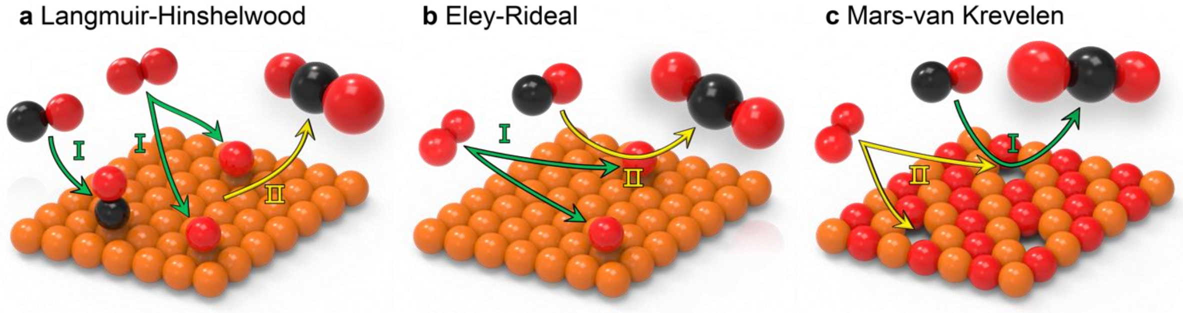

Figure 1.2. Schematic illustrations of (a) Langmuir–Hinshelwood mechanism, (b) Eley–Rideal mechanism and (c) Mars–van Krevelen mechanism.

1.2 References

1. Y. Sun, et al., Plasma-Catalytic CO2 Hydrogenation over a Pd/ZnO Catalyst: In Situ Probing of Gas-Phase and Surface Reactions, *JACS Au*, **2**, 1800-1810 (2022).
2. D.-Y. Kim, et al., Cooperative Catalysis of Vibrationally Excited CO2 and Alloy Catalyst Breaks the Thermodynamic Equilibrium Limitation, *J. Am. Chem. Soc.*, **144**, 14140-14149 (2022).
3. X. Chen; Sheng, Z.; Murata, S.; Zen, S.; Kim, H.-H. & Nozaki, T., CH4 dry reforming in fluidized-bed plasma reactor enabling enhanced plasma-catalyst coupling, *J. CO_2 Util.*, **54**, 101771 (2021).
4. Z. Sheng; Watanabe, Y.; Kim, H.-H.; Yao, S. & Nozaki, T., Plasma-enabled mode-selective activation of CH_4 for dry reforming: first touch on the kinetic analysis, *Chem. Eng. J.*, **399**, 125751 (2020).
5. P. Mehta; Barboun, P. M.; Engelmann, Y.; Go, D. B.; Bogaerts, A.; Schneider, W. F. & Hicks, J. C., Plasma-catalytic ammonia synthesis beyond the equilibrium limit, *ACS Catal.*, **10**, 6726-6734 (2020).
6. Y. Wang, et al., Shielding protection by mesoporous catalysts for improving plasma-catalytic ambient ammonia synthesis, *J. Am. Chem. Soc.*, **144**, 12020-12031 (2022).
7. P. Mehta; Barboun, P.; Herrera, F. A.; Kim, J.; Rumbach, P.; Go, D. B.; Hicks, J. C. & Schneider, W. F., Overcoming ammonia synthesis scaling relations with plasma-enabled catalysis, *Nat. Catal.*, **1**, 269-275 (2018).
8. J. C. Whitehead, Plasma–catalysis: the known knowns, the known unknowns and the unknown unknowns, *J. Phys. D: Appl. Phys.*, **49**, 243001 (2016).
9. E. C. Neyts; Ostrikov, K.; Sunkara, M. K. & Bogaerts, A., Plasma catalysis: synergistic effects at the nanoscale, *Chem. Rev.*, **115**, 13408-13446 (2015).
10. H.-H. Kim; Teramoto, Y.; Ogata, A.; Takagi, H. & Nanba, T., Plasma catalysis for

environmental treatment and energy applications, *Plasma Chem. Plasma Process.*, **36**, 45-72 (2016).

11. E. C. Neyts, Plasma-surface interactions in plasma catalysis, *Plasma Chem. Plasma Process.*, **36**, 185-212 (2016).
12. S. Xu; Chen, H.; Hardacre, C. & Fan, X., Non-thermal plasma catalysis for CO2 conversion and catalyst design for the process, *J. Phys. D: Appl. Phys.*, **54**, 233001 (2021).
13. A. Bogaerts, et al., The 2020 plasma catalysis roadmap, *J. Phys. D: Appl. Phys.*, **53**, 443001 (2020).
14. A. George; Shen, B.; Craven, M.; Wang, Y.; Kang, D.; Wu, C. & Tu, X., A Review of Non-Thermal Plasma Technology: A novel solution for CO2 conversion and utilization, *Renew. Sust. Energy Rev.*, **135**, 109702 (2021).
15. R. Snoeckx & Bogaerts, A., Plasma technology–a novel solution for CO 2 conversion?, *Chem. Soc. Rev.*, **46**, 5805-5863 (2017).
16. A. Bogaerts & Neyts, E. C., Plasma technology: an emerging technology for energy storage, *ACS Energy Lett.*, **3**, 1013-1027 (2018).
17. K. H. Rouwenhorst; Engelmann, Y.; van‘t Veer, K.; Postma, R. S.; Bogaerts, A. & Lefferts, L., Plasma-driven catalysis: green ammonia synthesis with intermittent electricity, *Green Chem.*, **22**, 6258-6287 (2020).

Chapter 2. Cooperative catalysis of vibrationally-excited CO_2 and alloy catalyst breaks the thermodynamic equilibrium limitation

The content of this chapter has been published in *J. Am. Chem. Soc.* [Kim. DY. et al *J. Am. Chem. Soc.* 144, 14140-14149 (2022).]

2.1 Abstract

Using nonthermal plasma (NTP) to promote CO_2 hydrogenation is one of the most promising approaches that overcome the limitations of conventional thermal catalysis. However, the catalytic surface reaction dynamics of NTP-activated species are still under debate. The NTP-activated CO_2 hydrogenation was investigated in Pd_2Ga/SiO_2 alloy catalysts and compared to thermal conditions. Although both thermal and NTP conditions showed close to 100% CO selectivity, it is worth emphasizing that when activated by NTP, CO_2 conversion not only improves more than 2-fold under thermal conditions but also breaks the thermodynamic equilibrium limitation. Mechanistic insights into NTP-activated species and alloy catalyst surface were investigated by using *in situ* transmission infrared spectroscopy, where catalyst surface species were identified during NTP irradiation. Moreover, in *in situ* X-ray absorption fine-structure analysis under reaction conditions, the catalyst under NTP conditions not only did not undergo restructuring affecting CO_2 hydrogenation but also could clearly rule out catalyst activation by heating. *In situ* characterizations of the catalysts during CO_2 hydrogenation depict that vibrationally-excited CO_2 significantly enhances the catalytic reaction. The agreement of approaches combining experimental studies and density functional theory (DFT) calculations substantiates that vibrationally-excited CO_2 reacts directly with hydrogen adsorbed on Pd sites while accelerating formate formation due to neighboring Ga sites. Moreover, DFT analysis deduces the key reaction pathway that the decomposition of

monodentate formate is promoted by plasma-activated hydrogen species. This work enables the high designability of CO_2 hydrogenation catalysts toward value-added chemicals based on the electrification of chemical processes via NTP.

2.2 Introduction

Regarding the problem of climate change caused by CO_2 and future fossil fuel depletion, the capture, utilization, and storage of carbon dioxide, a representative global warming gas, offers significant benefits in reducing CO_2 emissions[1-3]. In particular, CO_2 capture and utilization (CCUS) is considered a sustainable technology in addition to reducing emissions, which can provide synthetic fuels and chemicals using CO_2 as a feedstock[4,5]. In this regard, CO_2 hydrogenation with renewable H_2 is being proven as an alternative fuel production technology[6,7]. Therefore, achieving a proper understanding of CO_2 hydrogenation and rational design of catalysts to improve conversion and selectivity efficiencies is an important task. Recent reviews focused on selective CO_2 conversion of heterogeneous catalysts in CO_2 hydrogenation[8,9]. Meanwhile, for CO_2 hydrogenation, multimetallic catalysts can control CO_2- and hydrogen-bonding sites, charge transfer, and electronic structure properties through interactions between different monometallic catalysts, so the activity can be improved significantly over a monometallic catalyst[10-13]. In addition, nonthermal plasma (NTP) is considerably superior in activating thermodynamically stable molecules (e.g., CO_2, CH_4, and N_2): NTP-assisted catalysis is recognized as a promising technology that can overcome the thermodynamic limitation or formation of new reaction pathways that cannot be achieved with thermal catalysis[14-19]. CO_2 hydrogenation to CO is endothermic, and a high temperature is needed thermodynamically. Meanwhile, high temperatures would be detrimental to multimetallic catalysts, especially alloy catalysts, because the high-temperature situation would induce irreversible phase separation of each metallic element which permanently deteriorates the activity of multimetallic catalysts[20-22]. NTP enables low-temperature activation of stable molecules, which accelerates the overall reaction rate without catalyst deactivation. Particularly, I focused on the Eley−Rideal (E−R) pathway where vibrationally activated CO_2 reacts directly with adsorbed hydrogen and promotes CO_2 conversion kinetically at low temperatures. The E−R pathway in CO_2 hydrogenation has been proven by the molecular beam study on Cu and Cu/ZnO well-defined surfaces[23,24]. In principle, CO_2 hydrogenation occurs via the E−R pathway with a small activation energy. However, the pre-exponential factor is quite small because formate formation is strongly coordinate- dependent and the bending-mode CO_2 vibration is critically important[24]. Such insight is quite courageous for efficient CO_2 conversion into formate, leading to final products such as methanol[25,26], methane[27,28], or CO[29,30]. However, at low temperatures, population of vibrationally-excited CO_2 is quite low and E−R is not anticipated, yielding a low CO_2 conversion. In the field of NTP-assisted catalysis, rationally designing catalysts that could enable more efficient interactions between NTP-activated species and catalysts remain a great challenge[14,31]. I propose an NTP-combined Pd_2Ga/SiO_2 alloy catalyst system which produces a copious amount of vibrationally-excited species and has been proven experimentally in our previous study in CH_4 dry reforming. NTP realizes two-temperature reaction conditions where the system is kept at low temperatures, while the vibrational temperature of CO_2 would increase higher than the gas temperature which interacts directly with adsorbed hydrogen. A similar reaction enhancement mechanism is studied by Mehta et al., showing that vibrationally-excited N_2 promotes ammonia synthesis over the metal catalyst[32]. Meanwhile, Xu et al. confirmed the exceptional stability of metal−organic frameworks under NTP-assisted catalysis, which is also applicable to our reaction system with increased stability of alloy catalysts via low-temperature catalysis enabled by NTP[33]. Here, I first present the kinetic study in which the combination of NTP and the alloy catalyst yielded enhanced CO_2 conversion beyond the thermodynamic equilibrium limitation that could not be achieved under thermal catalysis. Intermetallic Pd_2Ga was chosen as the catalyst because this material has been reported to be active for CO_2 conversion[34,35]. To gain mechanistic insight into the NTP-activated CO_2 and alloy catalyst interaction, I developed *in situ* transmission infrared (TIR) spectroscopy, where NTP is generated in the TIR cell, and surface species were identified during NTP irradiation. Furthermore, chemical and structural transitions of catalysts during CO_2 hydrogenation under both thermal and NTP conditions were investigated by *in situ*

X-ray absorption fine-structure (XAFS) analysis. Finally, through agreement between experimental and DFT calculation approach on the realistic model, I aim to provide fundamental mechanical insights into the role of vibrationally-excited CO_2 derived from NTP and alloy catalysts in significantly improving CO_2 hydrogenation.

2.3 Experiment section

2.3.1 Materials and characterization

The Pd_2Ga/SiO_2 (Pd/Ga = 2) catalysts were synthesized by the pore-filling (co-)impregnation method. $Pd(NO)_2(NH_3)_2$ (Kojima Chemicals, 4.765 wt % in HNO_3 solution, Cas no. 14852-83-6)[36] and $Ga(NO_3)_3 \cdot nH_2O$ (n = 7−9, Wako, 99.9%) were used as metal precursors. The loading amounts of Pd and Ga were fixed at 10 and 3.3 wt %, respectively (atomic ratio: Pd/Ga = 2). Aqueous solution of the metal precursor(s) was first added dropwise to SiO_2 (CARiACT G-6, Fuji Silysia, S_{BET} = 673 $m^2 g^{-1}$, grain size: 300−425 μm), so that the solutions just filled the pore of SiO_2 (ca. 1.6 mL of solution per g of SiO_2). The obtained mixtures were sealed by three pieces of plastic film and kept overnight at room temperature, followed by transferring to a round-bottom flask and subsequent freezing using liquid nitrogen. The frozen mixtures were dried in vacuum at ca. −5 °C and further dried in an oven at 90 °C overnight. The resulting powder was calcined at 500 °C for 1 h in dry air with a ramping rate of 20 °C min^{-1}. The calcined powder was then reduced under flowing H_2 (0.1 MPa, 50 mL min^{-1}) at 500 °C for 1 h with a ramping rate of 20 °C min^{-1}. After the reduction, the catalyst bed was purged with N_2 and then exposed to air very slowly (overnight) for passivation. The crystalline phase in the prepared catalysts was obtained using powder X-ray diffraction (MiniFlex 700+D/teX Ultra; Cu Kα X-ray source). The main diffraction patterns to the intermetallic Pd_2Ga phase were observed (Figure 2.1), indicating that the desired metallic phases were successfully formed. A small amount of monometallic Pd also remained as a minor phase. XAFS spectra of Pd_2Ga/SiO_2 and reference samples were recorded at the BL9A beamline of the photon factory (PF) for the Ga K-edge and at the NW10A beamline of the Photon Factory Advanced Ring (PF-AR) for the Pd K-edge, respectively, in the Institute of Material Structure Science (IMSS) of High Energy Accelerator Research Organization (KEK). The XAFS spectra were recorded in a transmission mode. The formation of intermetallic Pd_2Ga was also suggested by XAFS analysis, where Pd− Ga (Ga−Pd) interatomic bonds were observed in the EXAFS results (Figure 2.2 and Table 2.1). The morphology of the prepared catalysts was observed by transmission electron microscopy (TEM, JEOL, JEM- ARM200F NEOARM, 200 kV). High-angle annular dark-field scanning transmission electron microscopy (HAADF-STEM) with energy- dispersive X-ray spectroscopy (EDX) was performed. The HAADF-STEM images (Figure 2.3a) show that Pd_2Ga nanoparticles with a size smaller than 8 nm were dispersed on the SiO_2 support (Figure 2.3d). The corresponding EDX elemental mapping confirms that Pd and Ga are distributed closely uniformly, indicating the intermetallic interaction between them due to the formation of a intermetallic phase (Figure 2.3b,c). Moreover, in Figure 2.3e, two clear lattice fringes spacings of 2.18 and 1.90 Å are observed, which correspond to the (211) and (203) planes of Pd_2Ga, respectively, and the dihedral angle is measured to be 41°. Consequently, the series of characterization results confirm the successful formation of the desired Pd_2Ga intermetallic catalysts.

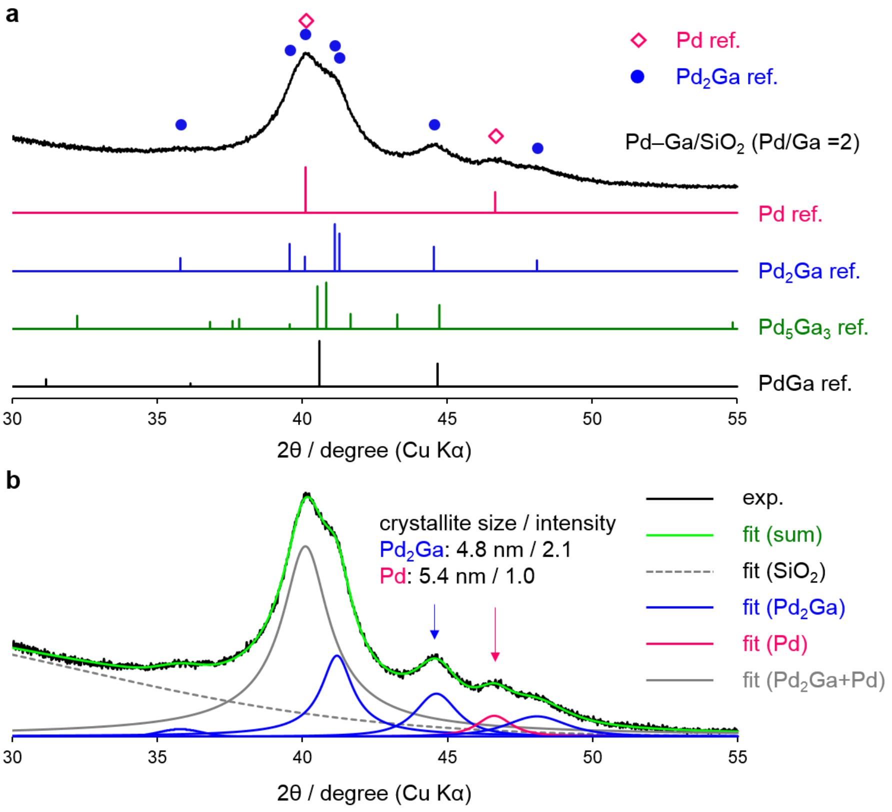

Figure 2.1. (a) XRD patterns of Pd-Ga/SiO_2. (Pd/Ga = 2) with the reference patterns of Pd and Pd-Ga intermetallic. (b) Peak deconvolution into the contribution of Pd, Pd_2Ga, and SiO_2. The crystallite sizes were determined using the Scherrer's equation for the peaks designated by arrows.

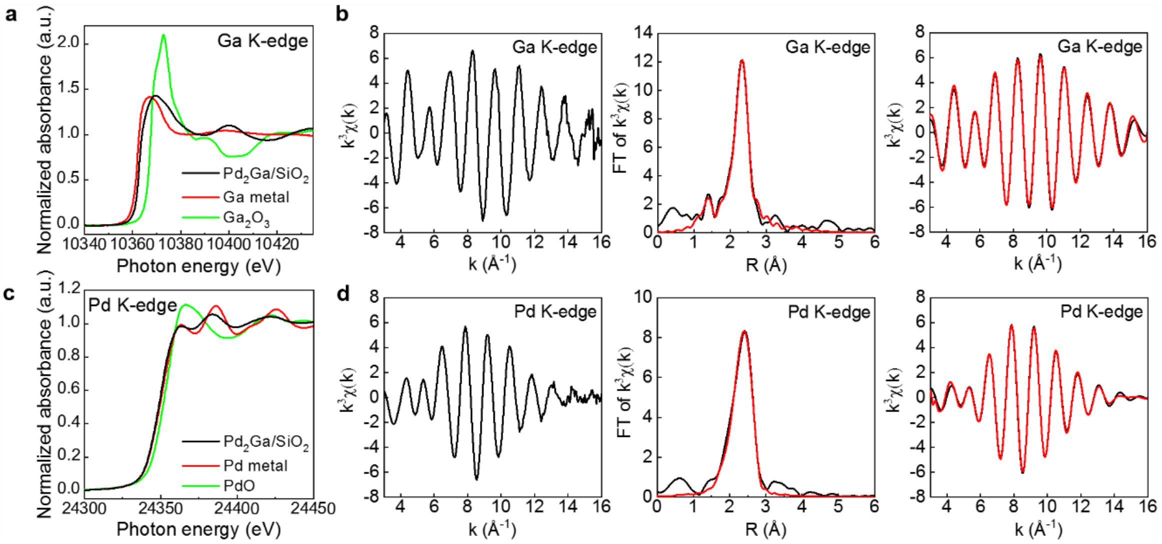

Figure 2.2. *In situ* XAFS results of the reduced Pd_2Ga/SiO_2. (a) Ga and (c) Pd K-edge XANES. (b) Ga and (d) Pd K-dege k^3-weighted EXAFS oscillation, Fourier-transformed (FT) EXAFS and inversely FT EXAFS are shown with the red fitted curves (see Table 2.1 for the details of the fitting). *k*-range for FT: 3.0−16.0 Å^{-1}. The measurements were carried out at room temperature in H_2 flow after reduction at 500 °C in H_2 flow for > 1 h. H_2 = 150 mL min^{-1}, pressure = 30 kPa.

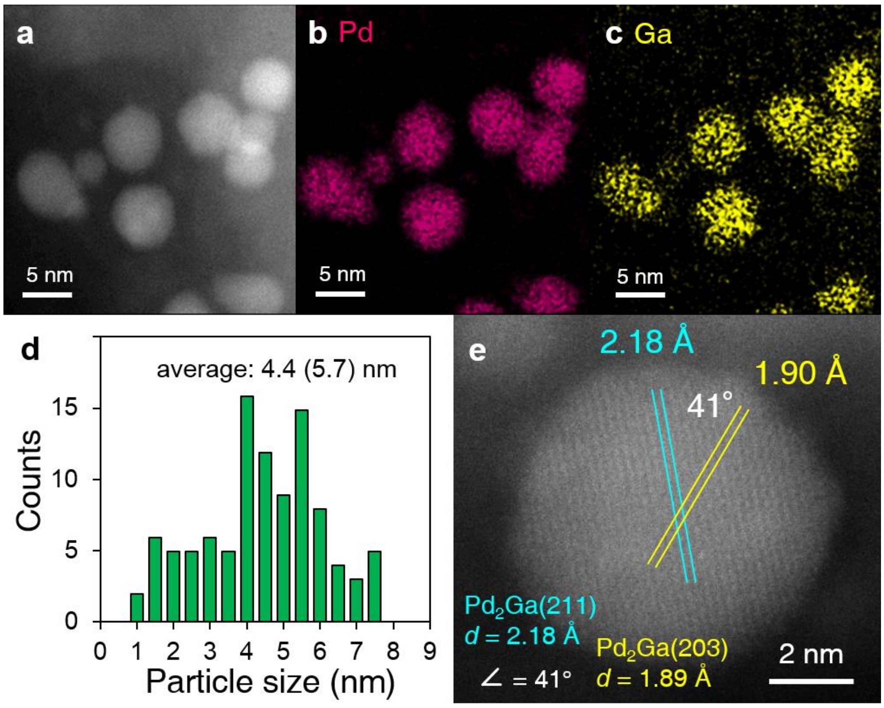

Figure 2.3. TEM image of Pd_2Ga/SiO_2. (a) HAADF-STEM image and the corresponding elemental maps of (b) Pd and (c) Ga acquired by EDX. (d) Particle size distribution. (e) High resolution HAADF-STEM image of single Pd_2Ga nanoparticle. The average in parathesis indicates the volume-weighted average.

Table 2.1. Curve-fitting results for Ga and Pd K-edge EXAFS data of the reduce Pd_2Ga/SiO_2 shown in Figure 2.2b and d, respectively[a]

Edge	Shell	N	r (Å)	ΔE (eV)	σ^2 (Å^2)	R-factor / %
Ga K	Ga-O	0.5 ± 0.2	1.77 ± 0.02	(-10)	0.0043 ± 0.0025	0.6
	Ga-Pd	3.6 ± 0.5	2.52 ± 0.02	0 ± 1	0.0075 ± 0.0003	
Pd K	Pd-Ga	1.4 ± 0.4	2.52 ± 0.02	(-9)	0.0083 ± 0.0025	0.7
	Pd-Pd	6.1 ± 1.0	2.76 ± 0.02	(-4)	0.0072 ± 0.0011	

[a] Parentheses indicate those values fixed during the fitting procedure. k-range for FT: 3.0-16.0 Å^{-1}. R-range for back k fitting: 1.1-2.9 Å and 1.6-3.9 Å for Ga and Pd K-edge EXAFS analysis, respectively.

2.3.2 Fluidized-bed dielectric barrier discharge

A fluidized-bed dielectric barrier discharge (FB-DBD) reactor was used for CO_2 hydrogenation over Pd_2Ga/SiO_2 (Figure 2.4). The quartz reactor (20 mm i.d. × 23 mm o.d.), ground electrode (aluminum), and furnace were laminated to have a better contact, while the high-voltage (H.V.) electrode (stainless steel; 1 mm i.d. × 6 mm o.d.) was coaxially placed along the axis of the reactor, creating 7 mm gas gap for generation of DBD. The H.V. electrode was immersed in the static catalyst powder. The feed gas was introduced from the tip of the H.V. electrode which blows off the catalyst powder, initiating a stable fluidization of catalysts. Before the CO_2 hydrogenation reaction, 4 g of Pd_2Ga/SiO_2 catalyst powder (300−425 μm) was reduced at 500 °C for 90 min in a 15% H_2/ Ar gas flow (total flow rate = 230 mL min^{-1}). The reduced catalyst powder was placed into the quartz reactor, and FB-DBD was applied by a gas mixture of H_2/CO_2 (molar ratio of 3:1). The total flow rate and the weight hourly space velocity (WHSV) of the gas mixture were 200 mL min^{-1} and 3000 mL g^{-1} h^{-1}, respectively, under STP conditions (25 °C and 101 kPa). For each test, the total pressure was fixed at 15 kPa. An AC high-voltage power source (Logy Electric; LHV-13AC, Vp-p = +8 to −6 kV, 12 kHz) was used to generate DBD. The applied voltage and the mean current were measured using an oscilloscope (Agilent Technologies; DSO-X 3014A). The discharge power was obtained by the voltage-charge Lissajous figure method and was fixed to 30 W in this study. The catalyst temperature was measured using the infrared camera combined with an IR-reflecting mirror (TH5104; NEC Sanei Instrument, Ltd). The infrared camera was calibrated by the thermocouples without DBD, showing an emissivity of 0.76 which represents most likely the temperature of the fluidized catalyst powder[15,37-40]. The gas analysis was performed using a quadrupole mass spectrometer (QMS, Prisma Plus QMG 220).

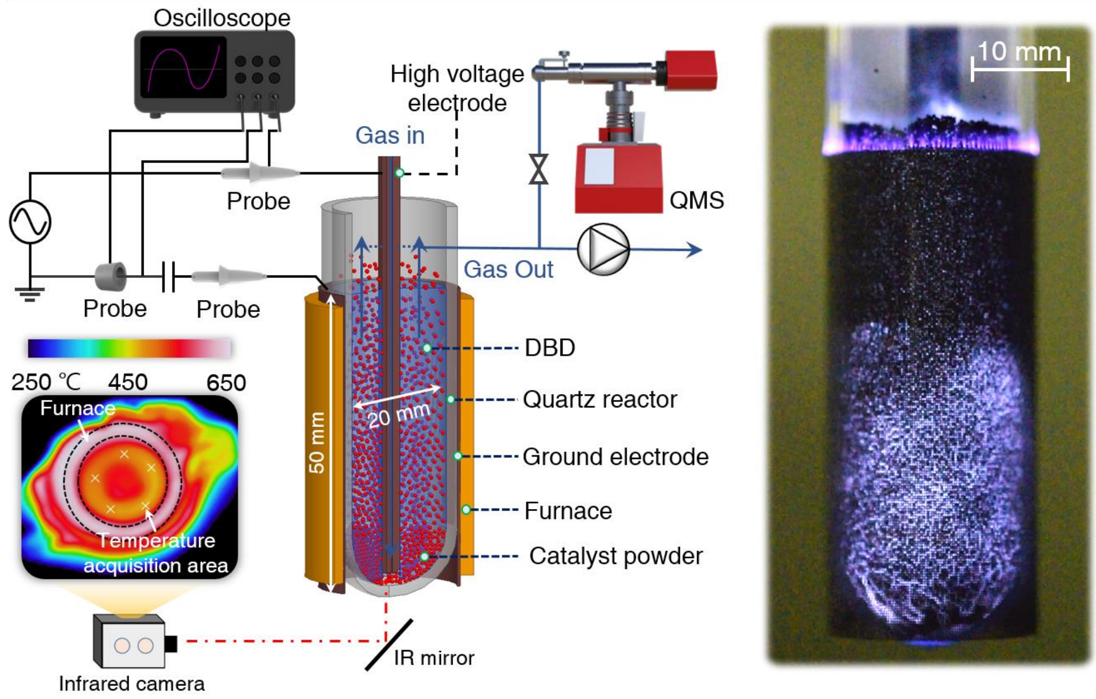

Figure 2.4. Schematic diagram of the FB-DBD reactor. Thermoimage (left side) represents the temperature distribution of fluidized Pd_2Ga/SiO_2 powder. Inset photograph (right side) represents discharge emission in FB-DBD reactor.

2.3.3 Kinetic analysis

I analyzed the mean reaction rate assuming continuous plug-flow reactor model in which the reaction rate is characterized by the inlet and the outlet of gas components. The power-law equation was integrated numerically by considering reaction orders to yield the mean rate constant. Lee et al. analyzed fluidize-bed reactor as either plug flow or mixed flow model.[41] They found a similar kinetic behavior between plug and mixed flow reactor models because the mean reaction rate was analyzed in both cases. Barea et al. performed systematic analysis of char gasification in a fluidized-bed reactor, concluding that the plug-flow condition of gas is necessarily needed to distinguish the kinetic effect from that of mass transfer and fluid motion[42]. Considering the similarity between our study and cited literature, our analytical method evaluating the mean reaction rate is rational.

Before the fluidization (gas flow is zero), DBD was not generated in the dense layer of catalyst powder due to the restriction of gas breakdown phenomena known as Paschen's law. Likewise, small gas flow rate near the "minimum fluidization velocity" does not generate DBD either in the powder layer. In order to generate DBD over the entire fluidized bed, a large gas flow to generate bubble-phase fluidization is necessary. Due to the fact that DBD is generated in the bubble-phase fluidization with large gas flow, back mixing is suppressed in our fluidized-bed plasma reactor.

CO_2 reaction rate was expressed by the power-law kinetics (eq 2.1). Take the natural logarithm of eq 2.1 and rewrite it into eqs 2.2−2.4.

$$-\frac{dP_{CO_2}}{dt} = r_{CO_2} = k_f {P_{CO_2}}^{\alpha} {P_{H_2}}^{\beta} \qquad \text{eq 2.1}$$

$$\ln r_{CO_2} = \ln k_f + \alpha \ln P_{CO_2} + \beta \ln P_{H_2} \qquad \text{eq 2.2}$$

$$\ln \frac{r_{CO_2}}{{P_{H_2}}^{\beta}} \propto \alpha \ln P_{CO_2} \qquad \text{eq 2.3}$$

$$\ln \frac{r_{CO_2}}{{P_{CO_2}}^{\alpha}} \propto \beta \ln P_{H_2} \qquad \text{eq 2.4}$$

Here, k_f and P expresses the forward reaction rate constant and the average concentration of CO_2 and H_2. α and β represent the modified reaction order for CO_2 and H_2, respectively. α and β were unknown figures at this point: Assume arbitrary values for α and β and performed iterative calculation until the deviation of α and β becomes smaller than 1% error. The feasibility of this method had been verified in our previous research on dry methane reforming[15].

Reaction order was estimated from Figure 2.5 at fixed total flow rate while varying H_2/CO_2 ratio without dilution gas. Figure 2.6 represents the corresponding CO_2 and H_2 conversion while ca. 100% CO selectivity was obtained in all cases. Experimental conditions are provided in the figure caption of Figure 2.6. In Figure 2.5, $\ln\frac{r_{CO_2}}{{P_{H_2}}^{\beta}}$ v.s. $\ln P_{CO_2}$ (a) and $\ln\frac{r_{CO_2}}{{P_{CO_2}}^{\alpha}}$ v.s. $\ln P_{H_2}$ (b) express the linear relationship; the slope of each line corresponds to the modified reaction order as summarized in Table 2.2. As presented in Figure 2.5, the reaction order of CO_2 and H_2 over Pd_2Ga/SiO_2 decreased clearly by applying DBD. First, smaller reaction order of H_2 than that of the thermal case implies the adsorption of H_2 is promoted by DBD. Second, smaller reaction order of CO_2 indicates the reaction probability between excited CO_2 and adsorbed H increases.

Apparent activation energy (E_{app}) of thermal and DBD catalysis was determined according to eqs 2-1 and 2-5.

$$k_f = Ae^{-\frac{E_{app}}{RT}} \qquad \text{eq 2.5}$$

The A, R and T represent pre-exponential factor, universal gas constant and catalyst temperature (K), respectively.

Specific energy input (SEI) was calculated by following eq 2.6

$$SEI\ (\text{eV molecule}^{-1}) = \frac{\text{Power (W)}}{eN_{\text{A}} \times \frac{Q_{\text{total}}^{\text{in}}}{60 \times 10^{6}} \times \frac{P}{RT}} \qquad \text{eq 2.6}$$

The $Q_{\text{total}}^{\text{in}}$ represents the total gas flow rate (mL min^{-1}, STP) at the reactor inlet; e = 1.602 × 10^{-19} (C); N_{A} = 6.02×10^{23}; R = 8.314 J K^{-1} mol^{-1}. Here, 1 eV molecule^{-1} is equivalent to

96.5 kJ mol^{-1}. CO_2 and H_2 conversion and CO selectivity were calculated by the following eqs 2.7–2.9.

$$CO_2 \text{ conversion } \% = \frac{F_{CO_2}^{in} - F_{CO_2}^{out}}{F_{CO_2}^{in}} \times 100 \qquad \text{eq 2.7}$$

$$H_2 \text{ conversion } \% = \frac{F_{H_2}^{in} - F_{H_2}^{out}}{F_{CO_2}^{in}} \times 100 \qquad \text{eq 2.8}$$

$$CO \text{ selectivity } \% = \frac{F_{CO_2}^{out}}{F_{CO_2}^{in} - F_{CO_2}^{out}} \times 100 \qquad \text{eq 2.9}$$

F (mol min^{-1}) expresses mol flow rate at STP conditions (25 °C and 101 kPa).

The average reaction rate (r_i; mol m^{-3}s^{-1}) was calculated using mole concentration of each species (P_i; mol m^{-3}) in eqs 2.10–2.12.

$$r_i = \frac{P_i^{in} - P_i^{out}}{\Delta t} \qquad \text{eq 2.10}$$

$$\Delta t = \frac{2V}{Q_{\text{total}}^{\text{in}} + Q_{\text{total}}^{\text{out}}} \qquad \text{eq 2.11}$$

$$V = V_0 - V_{cat} \qquad \text{eq 2.12}$$

The V_{cat} (= 2.1 mL) expresses the total volume of 4 grams of catalyst powders used for reforming.

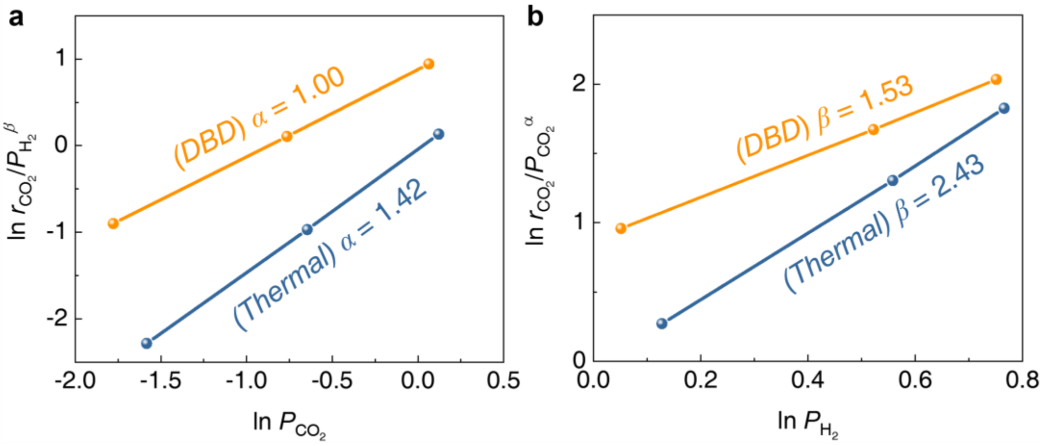

Figure 2.5. Modified reaction orders. (a) α for CO_2. (b) β for H_2, respectively. Conditions: see Figure 2.6 caption.

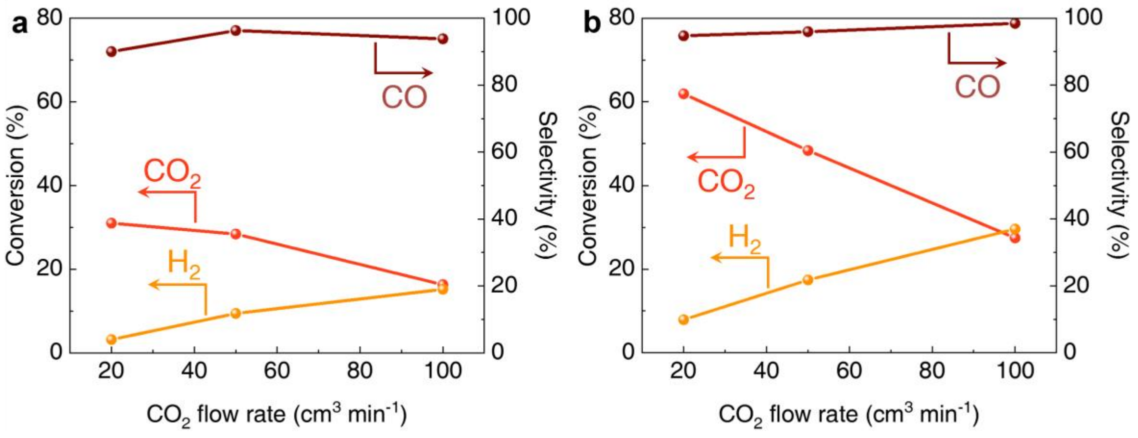

Figure 2.6. CO_2 and H_2 conversion (%) with respect to the initial CO_2 flow rate on 10 wt% Pd_2Ga/SiO_2. (a) Thermal catalysis. (b) DBD catalysis. Catalyst temperature and input power were fixed at 465 °C and SEI = 2.28 eV molecule^{-1}, respectively. Total flow rate = 200 mL min^{-1} (STP); H_2/CO_2 = 1, 3, and 9; WHSV = 3000 mL g^{-1} h^{-1} (STP); Pressure = 15 kPa.

Table 2.2. Modified reaction orders obtained from Figure 2.5.

	α	β
Thermal catalysis	1.42	2.43
DBD catalysis	1.00	1.53

2.3.4 *In situ* TIR

The *in situ* TIR characterization of catalyst CO_2 hydrogenation under plasma was measured using a DBD flow-type TIR cell under a pressure of 10 kPa (Figures 2.7 and 2.8). The *in situ* TIR cell was in the form of a cylindrical glass tube, and a K-type thermocouple (1 mm o.d.) was arranged to continuously monitor the temperature inside the reactor. The stainless-steel (1 mm o.d.) H.V. electrode and ground electrode were inserted inside the reactor. The ground electrode was wrapped in a quartz sheath. The electrical parameters of the DBD were monitored using an oscilloscope (RIGOL MSO5104) connected to the reactor via an H.V. probe. The gap between point-to-point electrodes was 10 mm. A high-voltage power supply was connected to the reactor and applied voltage and frequency for all catalyst tests were 2 kV and 19 kHz, respectively. The catalyst was powdered (25−30 mg), compressed with a pressure press, and manufactured in the form a pellet (10 mm o.d., 1 mm thickness). After that, the catalyst was fixed in a glass holder and inserted into the 5 mm downstream from the discharge zone. The *in situ* TIR spectra were collected using a Fourier-transform infrared spectrometer (FTIR, JASCO FTIR-6600) equipped with a mercury−cadmium−telluride (MCT) detector with 64 scans with a spectral resolution of 4 cm^{-1} in the range 4000−650 cm^{-1}. Spectra were recorded every 15 s. Background reference of the spectra of the reduced sample were acquired in a 6% H_2 in Ar flow. The catalyst pellet was reduced at 500 °C under a 6% H_2 in Ar flow for 1 h before testing. After reduction, the reactor was cooled to 250 °C under pure Ar. Then, CO_2 hydrogenation was performed by flowing CO_2 (10 mL min^{-1}) + H_2 (30 mL min^{-1}) diluted in Ar (150 mL min^{-1}). Furthermore, to gain insights into the evolution of surface species adsorbed on the catalysts during thermal and DBD conditions, transient experiments were performed by alternatingly flowing H_2/Ar (10/150 mL min^{-1}) and CO_2/Ar (10/150 mL min^{-1}). Ar was used as a balance gas to dilute the reaction gas and avoid signal saturation of IR spectra. The gas flow was controlled using a programable mass flow controller. The outlet gas stream of the reactor was measured using a QMS (Prisma Plus QMG 220) with a response time of ca. 1 s.

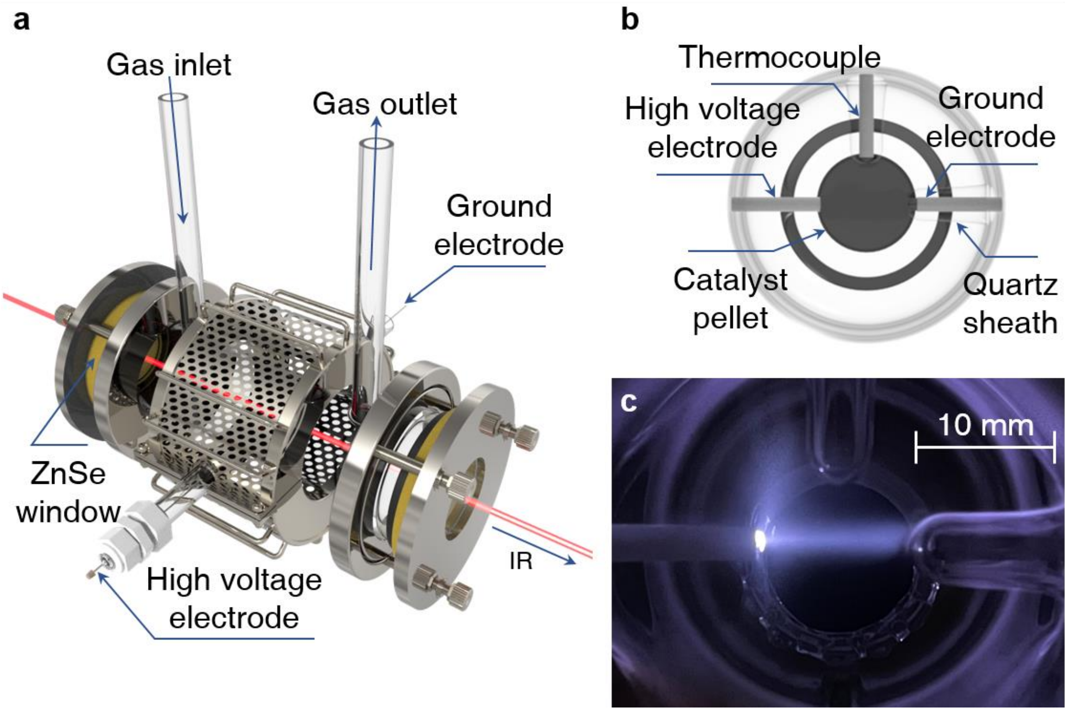

Figure 2.7. Design for the *in situ* DBD-TIR cell. (a) Schematic of the *in situ* TIR cell capable of identifying surface species with and without DBD irradiation characterized in this work (b) and (c) cross-sectional schematic (b) and a corresponding photograph (c) during DBD irradiation under CO_2 (10 mL min^{-1}) + H_2 (30 mL min^{-1}) diluted in Ar (150 mL min^{-1}). The high-voltage electrode is on the left exposing the metallic tip, while the grounded electrode is fully covered by glass sheath. The catalyst pellet is located behind the luminescence discharge channel which is separated by 5 mm to avoid direct contact of plasma channel to the catalyst surface.

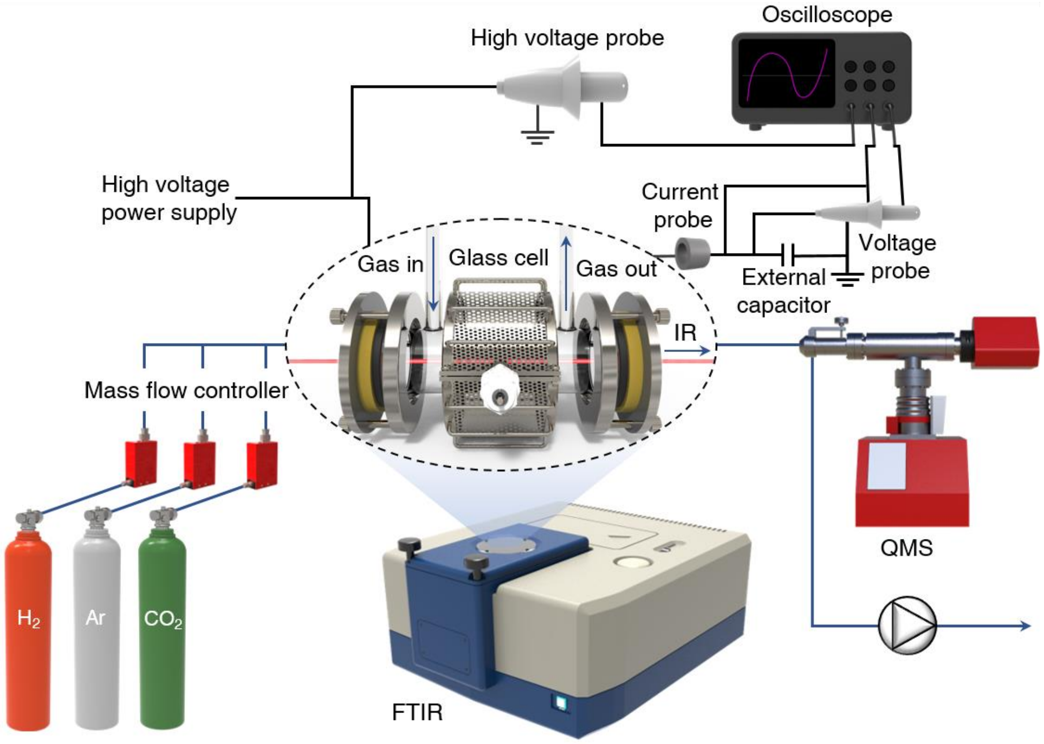

Figure 2.8. Schematic diagram of the experimental set up.

2.3.5 *In situ* XAFS

The *in situ* XAFS measurements were conducted using the identical TIR cell and experimental conditions shown in Figure 2.7 equipped with X-ray transparent windows made from Kapton (TX cell). Data analysis was performed with the REX 2000 software package (Rigaku Co., Japan). The XAFS oscillations $\chi(k)$ were extracted using a spline smoothing method and normalized to edge height, where k is the photoelectron wavenumber and calculated from the photon energy, E, using eq 2.1.

$$k = \sqrt{2m(E - E_0)/\hbar^2} \qquad \text{eq 2.1}$$

where E_0 and m are the threshold energy and the electron mass, respectively. The quantity $k^3\chi(k)$ was Fourier transformed to R space, the peak in the transform was filtered, and then an inverse Fourier transform was applied to convert the filtered peak back to k space. The Fourier-filtered data were then analyzed with a curve-fitting technique using the following theoretical XAFS eqs 2.2 and 2.3.

$$k^3\chi(k) = \sum_i \frac{k_i^2 S_i N_i F_i(k_i) e^{-2k_i^2\sigma_i^2} \sin(2k_i r_i + \varphi_i(k_i))}{r_i^2} \qquad \text{eq 2.2}$$

$$k_i = \sqrt{k^2 - 2m\Delta E_i/\hbar^2} \qquad \text{eq 2.2}$$

Here S_i, N_i, σi, r_i, and ΔE_i are the amplitude reduction factor, coordination number, Debye−Waller factor, bond distance of the ith bond, and energy shift in the origin of the photoelectron kinetic energy of the ith bond, respectively. The backscattering amplitude, $F_i(k)$, and phase shift, $\varphi_i(k)$ were calculated using the FEFF8.04 algorithm[43]. The amplitude reduction factors, S_i, were estimated using reference compounds or calculated using the FEFF8.04 algorithm.

2.3.6 Computational details

Periodic DFT calculations were performed using the CASTEP code[44] with Vanderbilt-type ultrasoft pseudopotentials and the revised version of Perdew−Burke−Ernzerhof exchange−correlation functional based on the generalized gradient approximation[45,46]. The plane-wave basis set was truncated at a kinetic energy of 360 eV. A Fermi smearing of 0.1 eV was utilized. Dispersion correlations were considered using the Tkatchenko−Scheffler method with a scaling coefficient of $s_R = 0.94$ and a damping parameter of $d = 20$[47]. The reciprocal space was sampled using a k-point mesh with a spacing of typically 0.04 $Å^{-1}$, as generated by the Monkhorst−Pack scheme[48]. Geometry optimizations were performed on supercell structures using periodic boundary conditions. I chose Pd_2Ga(020) plane as the most stable (likely to be exposed) and low-mirror index surface because of the clear appearance of the diffraction peak assignable to this plane (44.5°). The stronger the diffraction is, the higher the atom density is, hence the lower the surface energy is. The surfaces were modeled using the Pd_2Ga(020)-(2 × 1) metallic slabs with a thickness of four atomic layers with 13 Å of vacuum spacing. The unit cell size of the bulk material (Pd_2Ga) was first optimized, followed by modeling the slab structure and surface relaxation with the size of the supercell fixed. The convergence criteria for structure optimization and energy calculation were set to (a) an SCF tolerance of 1.0×10^{-6} eV per atom, (b) an energy tolerance of 1.0×10^{-5} eV per atom, (c) a maximum force tolerance of 0.05 eV $Å^{-1}$, and (d) a maximum displacement tolerance of 1.0×10^{-3} Å. For all calculations, the net charge was set to zero and spin polarization was considered. The adsorption energy was defined as follows: $E_{\mathrm{ad}} = E_{\mathrm{A-S}} - (E_{\mathrm{S}} + E_{\mathrm{A}})$, where $E_{\mathrm{A-S}}$ is the energy of the slab together with the adsorbate, E_{A} is the total energy of the free adsorbate, and E_{S} is the total energy of the bare slab. Transition-state search was carried out based on the complete linear synchronous transit/quadratic synchronous transit method[49,50] with the tolerance for all root-mean-square forces on an atom of 0.10 eV $Å^{-1}$.

2.4 Result and discussion

2.4.1 Kinetic study

I first carried out the kinetics study of CO_2 hydrogenation over Pd_2Ga/SiO_2 under both thermal and DBD conditions. The FB-DBD reactor was used for enhancing plasma catalyst interactions, as well as the heat and mass transport efficiencies[51].

Figure 2.9a shows the CO_2 conversion results over Pd_2Ga/SiO_2 with different Pd_2Ga loadings (10 and 3 wt %) under thermal and two types of DBD conditions which are generated by different frequencies (12 and 100 kHz) of power source. The CO_2 conversion increases with catalyst temperature, indicating similar trends under all conditions. In particular, in the case of both catalysts, the reaction activity was significantly improved under the DBD conditions compared to the thermal conditions. Meanwhile, SiO_2 and without catalyst (blank) is inactive under both thermal and DBD conditions (Figure 2.10). The CO selectivity was ca. 100% for all conditions (Figure 2.11). It is also worth highlighting that CO_2 conversion for 10 wt % Pd_2Ga/SiO_2 under 100 kHz DBD conditions is higher than the thermodynamic equilibrium limitation. The dotted line indicates the equilibrium CO_2 conversion for the reverse water-gas shift (RWGS) reaction (H_2/CO_2 molar ratio of 3) based on ground-state CO_2 at 15 kPa. This limitation curve would shift toward higher value than the thermal equilibrium when CO_2 is excited primarily into vibrational states. Estimation of the Gibbs energy for vibrationally-excited CO_2, or nonequilibrium two-temperature system (vibrational temperature > gas temperature), is not readily available. Assuming three fundamental vibration modes of CO_2 (bending, symmetric, and asymmetric stretching) with Boltzmann distribution of vibrational energy, approximately 34 mol % of CO_2 is excited into bending mode vibration at an equilibrium vibrational temperature of 1000 K. Such a unique condition is readily available in NTP without gas heating. Subsequently, bending-mode CO_2 would contribute additional conversion, yielding higher CO_2 conversion than that of the ground-state CO_2. As for the corresponding Arrhenius plot (Figure 2.9b), regardless of the Pd_2Ga loadings, the extracted activation energy for the DBD conditions is clearly smaller than that of the thermal conditions. The activation energy of four NTP reactions does not change to a large degree. In other words, DBD conditions can be grouped together (the activation energy is determined as ca. 43 kJ mol^{-1}). This implies that the reaction pathways, or the rate-determining step, for the two catalysts is not only identical but also not influenced by the concentration of vibrationally-excited molecules. Moreover, from the fact that the slopes of Arrhenius plots for all of the NTP reactions can consist of one group, even if, for 10 wt % Pd_2Ga/SiO_2, CO_2 conversion goes beyond the thermodynamic equilibrium limitation, it may not be con- strained by the reverse reaction. The remarkable activity of 10 wt % Pd_2Ga/SiO_2 under DBD conditions is further highlighted by comparison with mono-metallic catalysts (10 wt % Pd/SiO_2 and 3.3 wt % Ga/SiO_2). Comparing the CO yield over the three catalysts (Figure 2.12), under both DBD and thermal conditions, CO yield for 10 wt % Pd_2Ga/SiO_2 is much greater than the sum of the individual contribution of Pd and Ga catalysts. Moreover, the reaction is further enhanced under a DBD environment: the remarkable improvement in CO yield over Pd_2Ga/SiO_2 further highlights the synergistic effect of Pd_2Ga and DBD coupling. For Pd_2Ga/SiO_2, the tuning of the electronic structure of Pd by Ga can change the reaction barrier and catalyzing the reaction at a certain step, promoting intrinsic activity. This remarkable improvement in CO yield over Pd_2Ga/SiO_2 makes the synergistic effect of intermetallic Pd_2Ga and bending mode CO_2 more noteworthy.

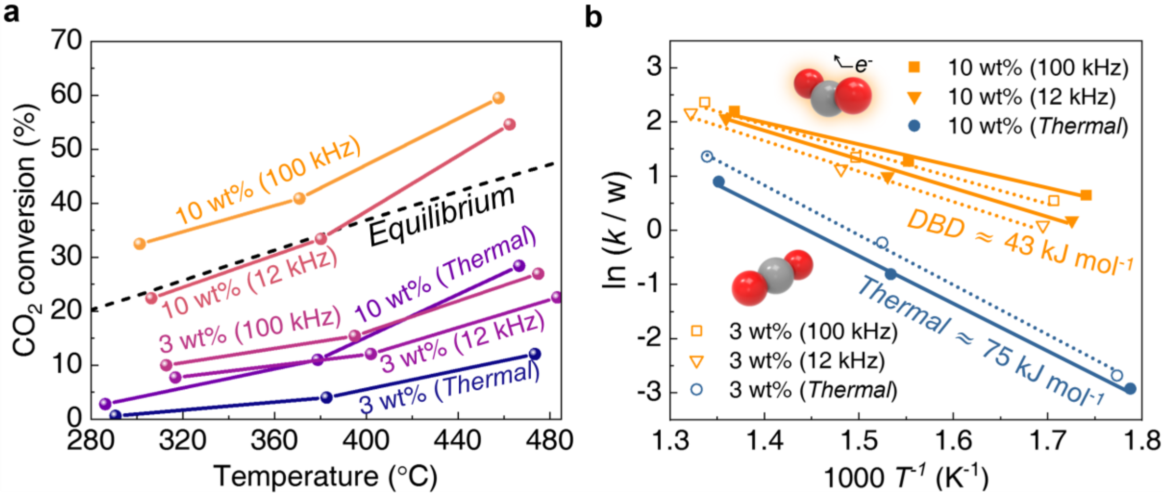

Figure 2.9. Kinetic study of CO_2 hydrogenation over the 10 and 3 wt % Pd_2Ga/SiO_2 with the FB-DBD reactor. (a) CO_2 conversion under thermal and DBD (12 and 100 kHz) conditions. (b) Arrhenius plot. Total flow rate = 200 mL min^{-1} (STP); $H_2/CO_2 = 3$; WHSV = 3000 cm^3 g^{-1} h^{-1} (STP); pressure = 15 kPa; and SEI = 2.28 eV molecules^{-1}.

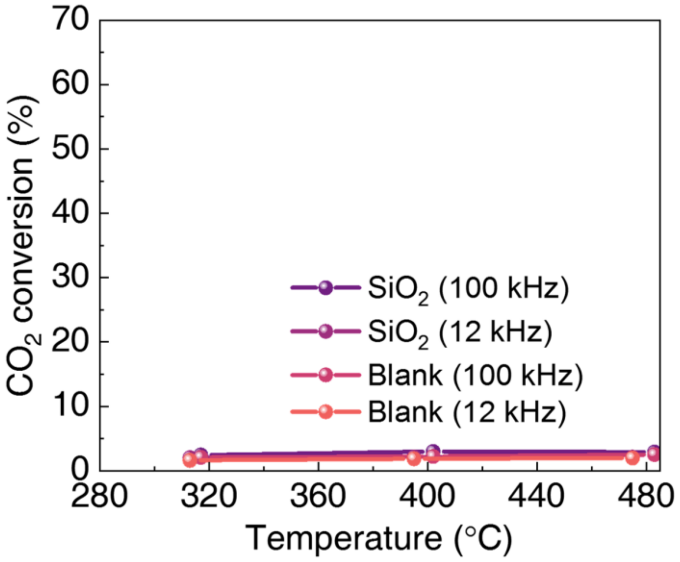

Figure 2.10. CO_2 conversion over SiO_2 and without catalyst (Blank) under DBD (12 and 100 kHz) conditions with the FB-DBD reactor.

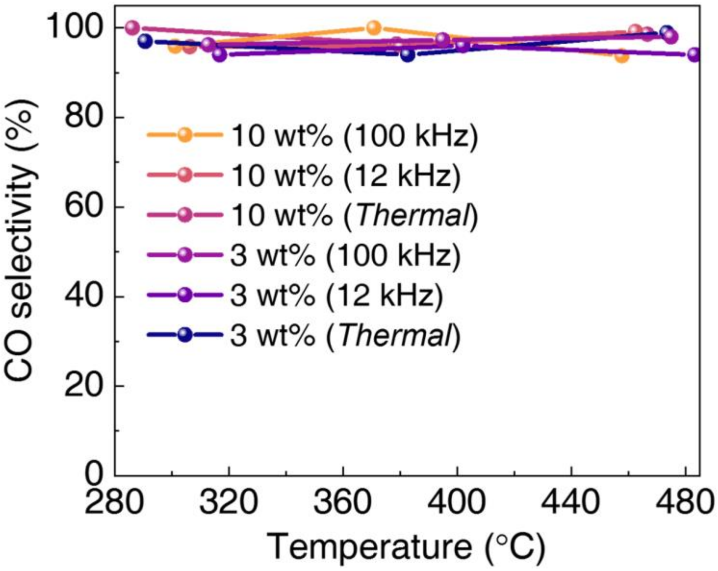

Figure 2.11. CO selectivity over the Pd_2Ga/SiO_2 corresponding to Figure 2.9.

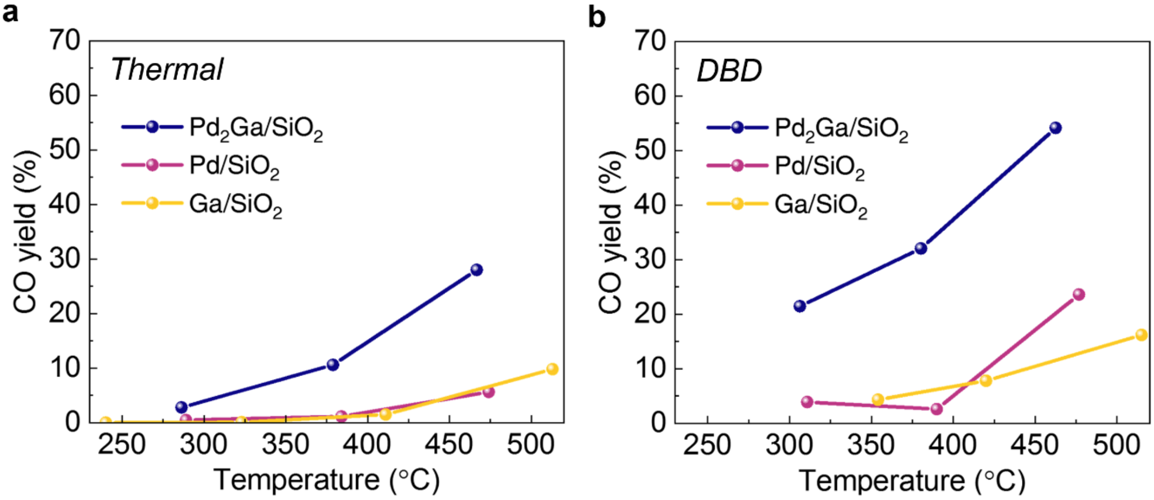

Figure 2.12. CO yield in CO_2 hydrogenation under thermal and 12 kHz DBD conditions over the 10 wt% Pd_2Ga/SiO_2, 10 wt% Pd/SiO_2 and 3.3 wt% Ga/SiO_2 with the FB-DBD reactor. (a) Thermal conditions. (b) DBD conditions.

2.4.2 Steady-state *in situ* TIR

The surface-adsorbed species were investigated for the Pd_2Ga/SiO_2 alloy catalyst using uniquely designed *in situ* TIR (Figure 2.7). Catalyst reaction experiments were conducted under both the thermal (at 250 °C) and DBD conditions. First, I performed steady-state experiments with a $CO_2 + H_2$ mixture. Figure 2.13 shows a series of *in situ* TIR spectra with and without DBD irradiation. Under the thermal conditions ($0 \text{ min} < t < 8 \text{ min}$), the catalyst can confirm the weak evolution of adsorbed CO over time. When the conditions changed from thermal to DBD at $t = 8$ min, two adsorbed peaks become intense remarkably, confirming the reaction promotion by DBD. IR peaks appear at 2077 and 1947 cm^{-1}, which are assigned to monocoordinated linearly and dicoordinated bridging bonded CO (denoted as CO_L and CO_B) at the Pd site, respectively[52-54]. Upon switching back from the DBD to the thermal conditions ($t = 16$ min), an abrupt decrease in each peak is observed. In general, the CO adsorption properties and reactivity of multimetallic to monometallic catalysts can be determined by the distribution of surface atoms: geometric ensemble effect and changes in the electronic structure due to monometallic interactions: ligand effect[55-58]. The absence of triply coordinated bridging CO on hollow sites[59,60] in the Pd_2Ga/SiO_2 indicates that the two metallic atoms, Pd and Ga, are well bonded and most of the surface-active sites contribute to the Pd_2Ga. Moreover, the properties of the CO adsorption and desorption can be attributed to the stronger ligand effect of Ga on individual Pd atoms[61]. Other clear adsorbed species, except adsorbed CO, were not observed suggesting rapid formation and decomposition of reaction intermediates. Meanwhile, DBD can not only vibrationally-excite gas-phase CO_2 but also dissociate it to CO[14,18,31,62]. Therefore, the adsorbed CO species under the DBD conditions may not fully rule out the effect of gas-phase CO_2 dissociation to CO. I performed additional experiments combined with QMS analysis (Figure 2.14), showing that gas-phase CO generation is negligible because plasma input power was set 0.1 W so that the energy density becomes as small as 0.77 kJ mol^{-1}. DBD-induced unique reaction behavior originates from the surface reaction.

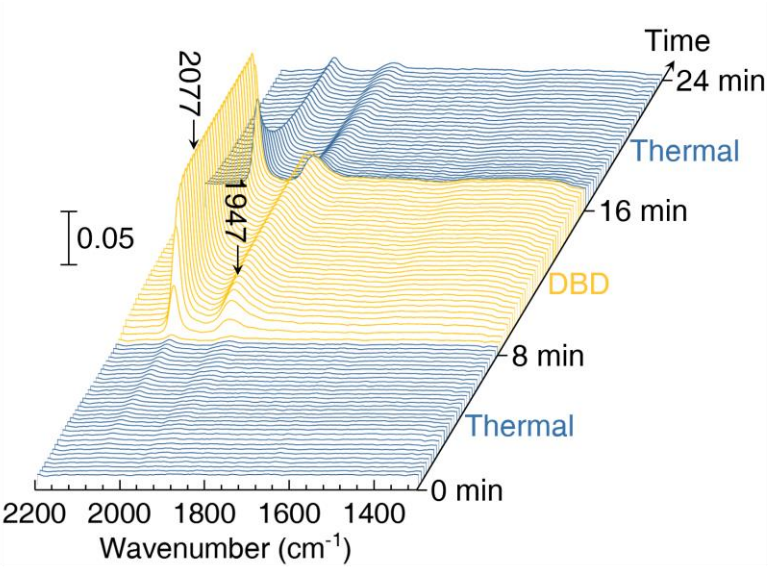

Figure 2.13. Plasma enhancement of CO_2 hydrogenation identified by *in situ* TIR. *In situ* TIR spectra of surface species on Pd_2Ga/SiO_2. A $CO_2 + H_2$ mixture was introduced at a constant flow rate, while reaction conditions were switching from thermal to DBD to thermal for every 8 min.

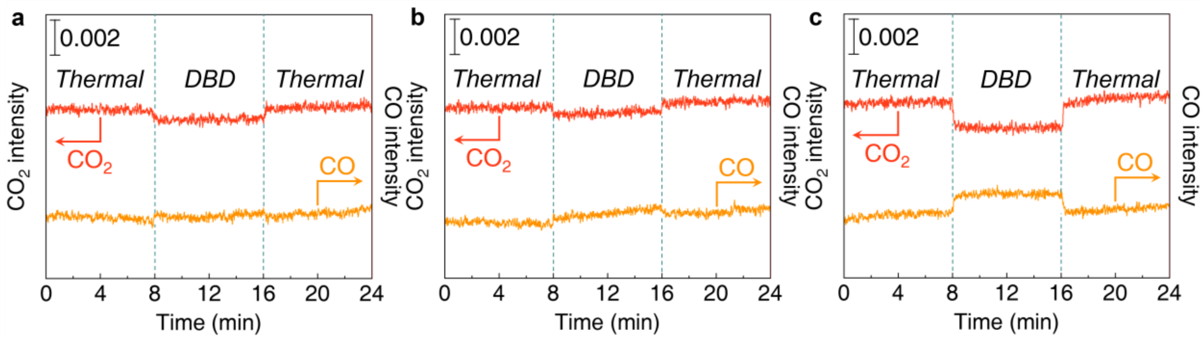

Figure 2.14. Identification of the influence of gas phase CO_2 dissociation to CO under DBD conditions with QMS. QMS signal over the (a) Blank, (b) SiO_2 and (c) Pd_2Ga/SiO_2 at 250 °C under CO_2 (10 mL min^{-1}) + H_2 (30 mL min^{-1}) diluted in Ar (150 mL min^{-1}). DBD was turned on from 8 min to 12 min, comparing thermal and DBD hybrid reactions. To clarify the influence of the DBD-induced gas phase reaction, under the thermal and DBD transient experiments over the without catalyst (Blank), SiO_2, and Pd_2Ga/SiO_2 with CO_2 + H_2 mixture QMS studies were performed. Under these conditions, the plasma power was 0.1 W. Upon turning on DBD, a CO signal was not detected by QMS with Blank experiment. In the case of SiO_2, compared to the Blank experiment, a faint CO signal was observed by QMS, indicating that CO_2 dissociation to CO by DBD is not promoted. In contrast, in the case of Pd_2Ga/SiO_2, a CO signal increased clearly during DBD treatment. Generation of CO originates DBD-induced catalyst reaction and gas phase CO_2 dissociation to CO by DBD is negligible.

2.4.3 Transient *in situ* TIR

To identify the reaction intermediates and to reach a deep insight into their reaction behavior, the transient *in situ* TIR was employed for DBD and thermal conditions over Pd_2Ga/SiO_2. In Figure 2.15a, similar to Figure 2.13, the CO_L and CO_B were observed upon introducing CO_2 at t = 6 min. After ca. 2 min, the CO_L and CO_B were fully desorbed, followed by a new IR peak appeared at 1368 cm^{-1}: the peak was assigned to an overlapped monodentate formate (m-HCOO) and bidentate formate (b-HCOO)[63-65]. When the feed gas was switched from CO_2 to H_2 at t = 12, the m-HCOO decreased immediately, but the b-HCOO (1355 cm^{-1}) did not change significantly. Continuing with the switching back from H_2 to CO_2 at t = 18 min, the same trend of adsorbed CO species was observed. I used SiO_2, which is generally regard as an inert support, and the surface species formed on SiO_2 could not be observed (Figure 2.16). The TIR spectra presented in Figure 2.15c show the evolution of the surface species with CO_2 + H_2 mixture and CO_2 under DBD conditions. When a CO_2 + H_2 mixture was introduced (0 min < t < 6 min) and when switching the gas stream from CO_2 + H_2 to CO_2 (6 min < t < 12 min), the IR peaks of adsorbed CO and HCOO were identical to those shown under the same conditions in Figures 2.13 and 2.15a, respectively. However, once the stream was switched back from CO_2 to CO_2 + H_2 mixture at 12 min, with an instantaneous decrease in m-HCOO, the evolution of adsorbed CO was observed, and significant change was not observed in b-HCOO, as presented in Figure 2.15d. Meanwhile, in Figure 2.15a, upon switching H_2 to CO_2 at 6 min, the sharp CO peak appears. On the other hand, when switching from CO_2 to H_2 at 12 min, the CO peak does not appear at all, indicating CO_2 and H_2 do not coexist at the moment of gas switching: the residual gas mixing effect is negligible in this study. Previously reported RWGS studies suggested that HCOO is the key intermediate surface species and that it decomposes by the H atom spillover from metallic particles[29,66-68]. The formation and desorption behavior of CO showed a correlation with m-HCOO. The adsorbed CO is formed from the decomposition of m-HCOO, and b-HCOO is quite stable at the reaction temperature.

Under the $CO_2 + H_2$ mixture, two points can be inferred from the absence of m- HCOO and b-HCOO: (i) from Figure 2.13, rapid formation and decomposition of m-HCOO through CO_2 hydrogenation over Pd_2Ga/SiO_2. (ii) From Figure 2.15a,c, reaction branching sequential from m-HCOO to b-HCOO or CO: adsorbed hydrogen is the key to determine the selectivity of b-HCOO and CO. When 6 min < t < 12 min (18 min < t < 24 min), there was an obvious shortage in hydrogen. Therefore, the formation of CO is suppressed and a sequential reaction from m-HCOO to b- HCOO occurs. This reaction pathway occurs under thermal conditions as well. In other words, the effect of DBD is highlighted during m-HCOO decomposition with sufficient surface hydrogen. All these observations are supported consistently by the DFT analysis as discussed later. Meanwhile, CO_2 is a molecule with a linear equilibrium structure in the ground-state, so it belongs to the $D \infty h$ symmetry group. The molecular orbital energy according to the bonding angle of CO_2 can be represented by a Walsh diagram[69,70] (Figure 2.17). The highest occupied molecular orbital (HOMO) is mainly confined to the terminal oxygen atom, while the antibonding lowest unoccupied molecular orbital (LUMO) is mostly located at the center of the carbon atom. Therefore, in this case, CO_2 can be considered an amphoteric molecule in which oxygen atoms exhibit Lewis basic properties and carbon atoms act as Lewis acid properties. CO_2 is an electron acceptor rather than a donor, and the reactivity of CO_2 depends on the electrophilic properties of the carbon atom. If the LUMO of CO_2 is filled through electron transfer, consequently the lowest energy state corresponds to a bent geometry. Obviously, this means that the CO_2-bending mode formed by the electron impact in the plasma environment can promote the catalytic surface reaction (e.g., by a reaction with the metal-hydride bond in which the metal center occupies the positive charge and the negative charge accumulates on the hydrogen). Recently, molecular beam study found that the OCO angle of vibrationally-excited CO_2 was much larger than the angle of the transition state (TS)[24]. In addition, based on DFT calculations, the bending vibration-driven CO_2 in HCOO formation occurs through the E−R pathway without barriers to the reaction with adsorbed hydrogen.

Indeed, it is possible to generate abundant vibrationally-excited CO_2 species by low-energy electron collision in DBD-type NTP and a lower reaction barrier is required for catalysis[15,16,40,71]. In other words, vibrationally- excited CO_2 generated in DBD under this experimental condition leads to the formation of CO_2-bending mode and can form HCOO by directly reacting with hydrogen adsorbed on the catalyst surface.

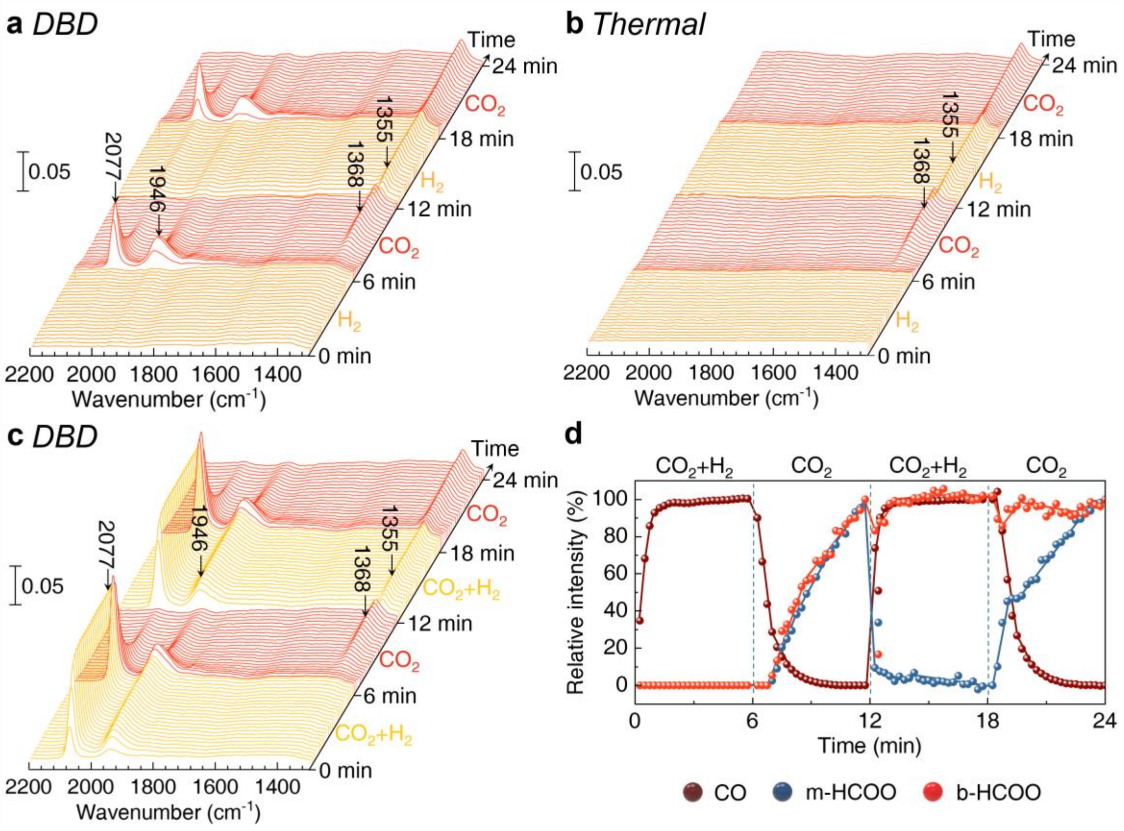

Figure 2.15. Identification of the reaction intermediates for CO_2 hydrogenation over Pd_2Ga/SiO_2. (a,b) *In situ* TIR spectra where the feed gas was switched alternately between H_2 and CO_2 for 6 min interval under the DBD (a) and thermal (b) conditions. (c) *In situ* TIR spectra where the feed gas was switched alternately between CO_2 + H_2 mixture and CO_2 for 6 min interval. (d) Relative intensities attributed to CO_L (2077 cm^{-1}), m-HCOO (1368 cm^{-1}), and b-HCOO (1355 cm^{-1}) in (c) as a function of time.

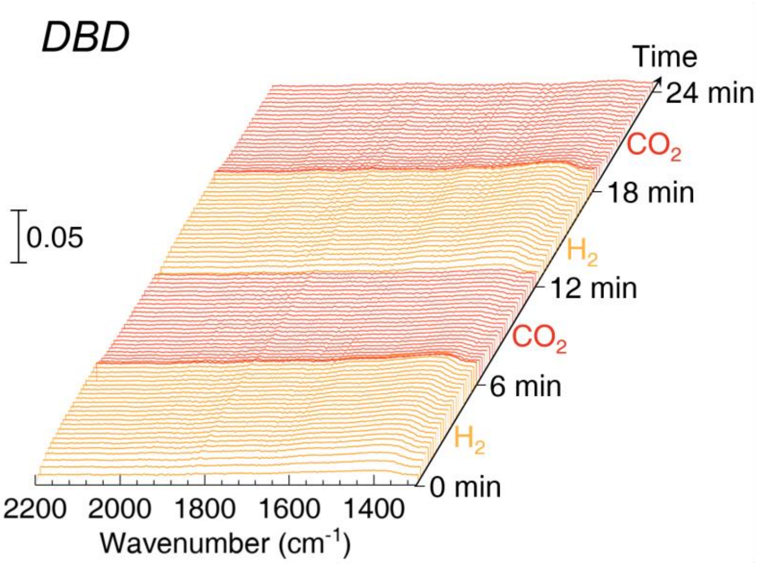

Figure 2.16. *In situ* TIR spectra over SiO_2 where the feed gas was switched alternately between H_2 and CO_2 for 6 min interval under the DBD conditions.

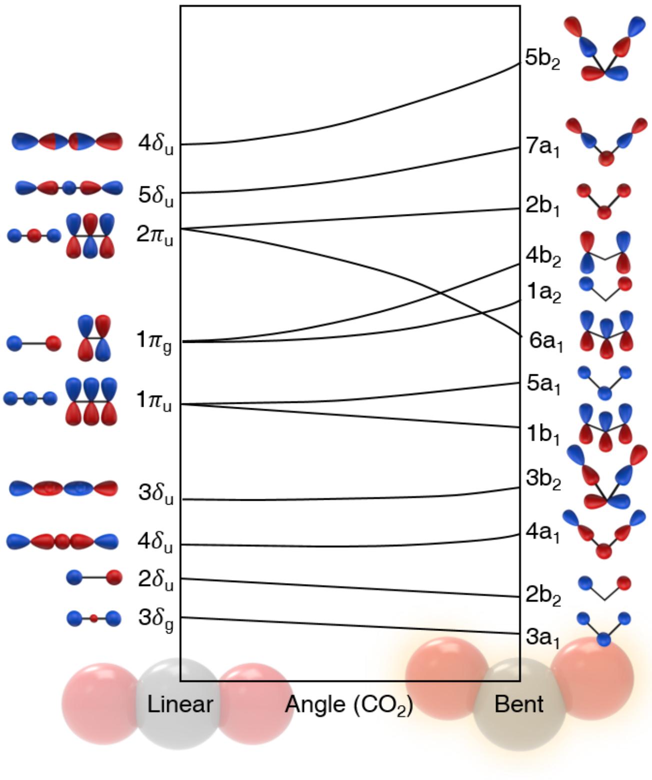

Figure 2.17. Walsh diagram of CO_2 orbital energies in linear and bent geometries[69,70]. Based on the linear geometry (180°), the schematics of the molecular orbitals are shown on the left side, and the symmetry properties of the orbital are shown on the right side. The molecular orbital most relevant to reactivity are the $1\pi_g$ and $2\pi_u$ orbitals roles as the highest occupied molecular orbital (HOMO) and the lowest unoccupied molecular orbital (LUMO), respectively. According to Walsh's rule, CO_2 adopts a linear shape. On the other hand, due to environmental factors, when LUMO is filled with electrons, the energy of the bent shape of CO_2 is more stabilized than linear shape. Also, the bending mode of vibrationally-excited CO_2 by plasma can induce changes in the shape and energy level of LUMO.

2.4.4 *In situ* XAFS

I cannot rule out the contribution of catalyst restructuring and heating by NTP[72], besides the vibrationally-excited CO_2, in the significantly promotional CO_2 hydrogenation upon the NTP conditions. Therefore, I performed *in situ* Ga and Pd K-edge XAFS measurements to observe local structure around Ga and Pd atoms under both thermal and NTP conditions during the CO_2 hydrogenation.

The XANES and EXAFS spectra under thermal and NTP conditions did not show a significant difference for both Ga and Pd K-edge (Figure 2.18). The curve-fitting results of the EXAFS spectra shown in Tables 2.3 and 2.4 revealed that all the structural parameters such as the coordination number (*N*), bond distance (*r*), and square of Debye−Waller factor (σ^2) were similar between thermal and NTP conditions within the margin of errors, suggesting that no catalyst restructuring was induced by NTP. It should be noted that no catalyst heating took place by NTP since the σ^2 value did not change within the margin of errors under the thermal and NTP conditions[72]. Thus, the catalyst did not undergo any structural changes or heating affecting the NTP-assisted CO_2 hydrogenation. The *in situ* XAFS results strongly indicated that the significantly improved CO_2 hydrogenation by the NTP-combined catalyst system was achieved by vibrationally-excited CO_2.

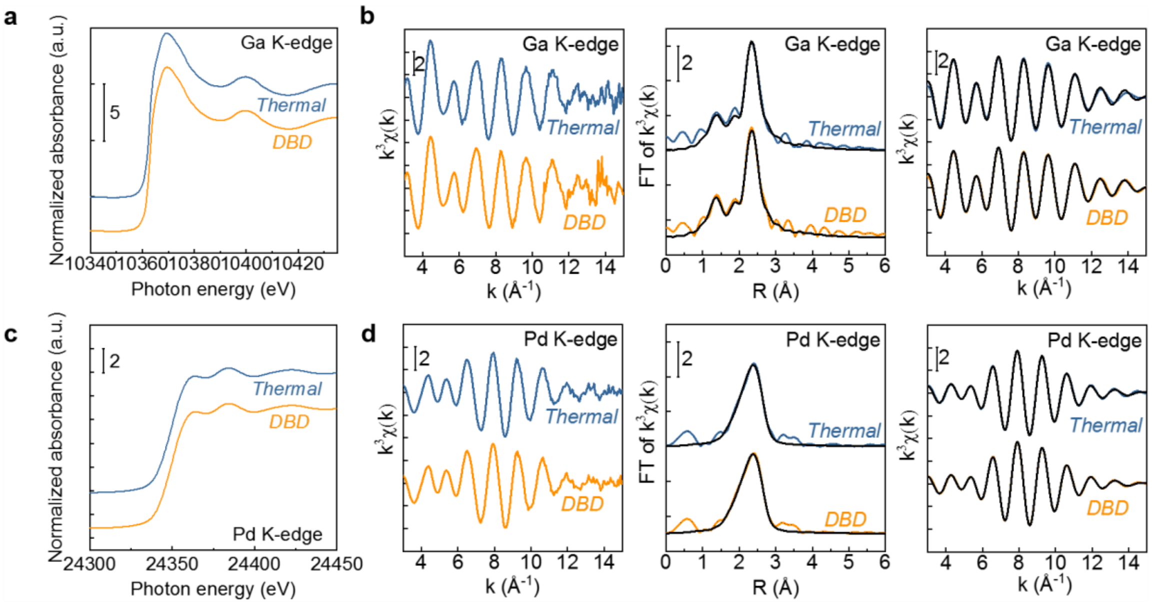

Figure 2.18. *In situ* XAFS results of the Pd_2Ga/SiO_2 during CO_2 hydrogenation with and without DBD. (a) Ga and (c) Pd K-edge XANES. (b) Ga and (d) Pd K-edge k^3-weighted EXAFS oscillation, Fourier−transformed (FT) EXAFS and inversely FT EXAFS data are shown with the black fitted curves (see Tables 2.3 and 2.4 for the details of the fitting). *k*-range for FT: 3.0−15.0 Å^{-1}; Ar = 100 mL min^{-1}; H_2 = 30 mL min^{-1}; CO_2 = 10 mL min^{-1}; pressure = 10 kPa; Reaction temperature = 250 ºC.

Table 2.3. Thermal reaction: Curve-fitting results for Ga and Pd K-edge EXAFS data of the Pd_2Ga/SiO_2 during CO_2 hydrogenation (curves shown in Figure 2.18b and d)[a]

Edge	Shell	N	r (Å)	ΔE (eV)	σ^2 (Å^2)	R-factor / %
Ga K	Ga-O	0.7 ± 0.2	1.77 ± 0.02	(-10)	0.0071 ± 0.0019	0.8
	Ga-Pd	3.6 ± 0.3	2.51 ± 0.02	-1 ± 2	0.0114 ± 0.0008	
Pd K	Pd-Ga	1.7 ± 0.3	2.53 ± 0.02	(-9)	0.0119 ± 0.0013	0.2
	Pd-Pd	6.6 ± 0.7	2.74 ± 0.02	(-4)	0.0117 ± 0.0009	

[a]Parentheses indicate those values fixed during the fitting procedure. *k*-range: 3.0-15.0 Å^{-1}. *R*-range for back *k* fitting: 1.1-2.9 and 1.6-3.0 Å for Ga and Pd K-edge EXAFS analysis, respectively.

Table 2.4. DBD reaction: Curve-fitting results for Ga and Pd K-edge EXAFS data of the Pd_2Ga/SiO_2 during CO_2 hydrogenation (curves shown in Figure 2.18b and d)[a]

Edge	Shell	*N*	*r* (Å)	Δ*E* (eV)	σ^2 (Å^2)	R-factor / %
Ga K	Ga-O	0.7 ± 0.2	1.76 ± 0.02	(-10)	0.0064 ± 0.0014	0.3
	Ga-Pd	3.4 ± 0.3	2.51 ± 0.02	0 ± 1	0.0110 ± 0.0008	
Pd K	Pd-Ga	1.8 ± 0.2	2.52 ± 0.02	(-9)	0.0125 ± 0.0009	0.1
	Pd-Pd	6.7 ± 0.4	2.74 ± 0.02	(-4)	0.0121 ± 0.0005	

[a] Parentheses indicate those values fixed during the fitting procedure. *k*-range for FT: 3.0-15.0 Å^{-1}. *R*-range for back *k* fitting: 1.1-2.9 Å and 1.6-3.0 Å for Ga and Pd K-edge EXAFS analysis, respectively.

2.4.5 Computational study

In order to obtain more detailed understanding regarding the influence of Ga−Pd-alloyed surface on the catalytic activity, I investigated further by performing DFT calculations. Starting from hydrogen atoms adsorbed on the $Pd_2Ga(020)$ surfaces, the calculated energy diagram and the corresponding structures are shown in Figure 2.19. In this model, CO_2 is assumed to be a ground-state in linear geometry. For the $Pd_2Ga(020)$ surface, because our calculations show that the carboxyl (COOH) formation (blue pathway) and direct CO_2 decomposition (orange pathway) have a much higher energy barrier than the HCOO formation barrier (red pathway), these two pathways are ruled out. Therefore, I focus on the HCOO formation as the most favorable pathway. For the initial activation of $CO_2(g)$ to HCOO formation on the surface of the $Pd_2Ga(020)$ surface, the E−R and Langmuir−Hinshelwood (L−H) pathways were considered. In the E−R pathway (green pathway), initial hydrogen atoms adsorbed on the surface migrate to the top side (59.2 kJ mol^{-1}), and then $CO_2(g)$ reacts directly with the hydrogen to from m-HCOO (67.7 kJ mol^{-1}). While climbing the activation barrier for TS, the C atoms at the center of the CO_2 molecule attach directly to hydrogen adsorbed to the Pd site. Subsequently, one of the O atoms is attached to the neighboring Ga atom that has affinity of the O atoms[73]. On the other hand, in the L−H pathway (pea green pathway), a $CO_2(g)$ activation barrier of 52.2 kJ mol^{-1} for surface adsorption then reacts with adsorbed hydrogen to form m-HCOO (81.9 kJ mol^{-1}). Therefore, even under thermal conditions, the E−R pathway is more favorable than the L−H pathway for m-HCOO formation. The reaction of m-HCOO is branching to either b-HCOO formation or decomposition to CO, as discussed in Figure 2.15. The m-HCOO can be converted to b-HCOO via the bridge HCOO (br-HCOO, 31.3 kJ mol^{-1}) in which two O atoms are bounded on Ga atoms (Ga−Ga). Subsequently, b-HCOO is stabilized further on Ga and Pd (Ga−Pd) with an activation barrier of 4.4 kJ mol^{-1}. Because the energy barrier for the reverse reaction from b-HCOO to m-HCOO is so large, b- HCOO is quite stable: this is an agreement with *in situ* TIR (Figure 2.15d). The decomposition of m-HCOO undergoes a transformation from br-HCOO to side HCOO (s-HCOO), a form in which the C atom is bound to Pd atom lying down, and then is decomposed with an activation barrier of 74.1 kJ mol^{-1}. For Pd_2Ga(020), the nucleophilic Pd atom with the ligand effect by Ga could enhance the interaction by promoting electron transfer to the LUMO centered at the C atom. As discussed above, when CO_2 coordinates with the metal or metal-hydride bond and fill the LUMO with electrons, the CO_2 results in a bent form, which is a lower energy state. At this time, HOMO, which has a localized electron density as lone pairs of oxygen atoms, forms a bond with an electrophilic Ga atom[74]. Note that this consideration is based on a fully thermal reaction: E−R pathway should be enhanced much stronger when CO_2 is primarily excited to bending-mode vibration. These DFT calculation results are in good agreement with the *in situ* TIR results and can strongly support the proposed plasma-enhanced reaction mechanisms. Meanwhile, in the kinetic study, the apparent activation energy of thermal conditions was determined as ca. 75 kJ mol^{-1} (Figure 2.9b). This value is in good agreement with the DFT calculation (74.1 kJ mol^{-1}), identifying the rate- determining step in the thermal reaction is the decomposition of m-HCOO. Interestingly, the apparent activation energy of the DBD reaction is estimated to be ca. 43 kJ mol^{-1} which is smaller than the activation barrier for m-HCOO formation (67.7 kJ mol^{-1}) and decomposition (74.1 kJ mol^{-1}): not only HCOO formation via the E−R pathway but also HCOO decomposition is promoted by DBD. As discussed earlier, hydrogen spillover is essential to decompose HCOO to yield CO. The role of DBD is not limited to vibrational excitation of CO_2, but activation of H_2 toward enhanced hydrogen spillover is highly anticipated.

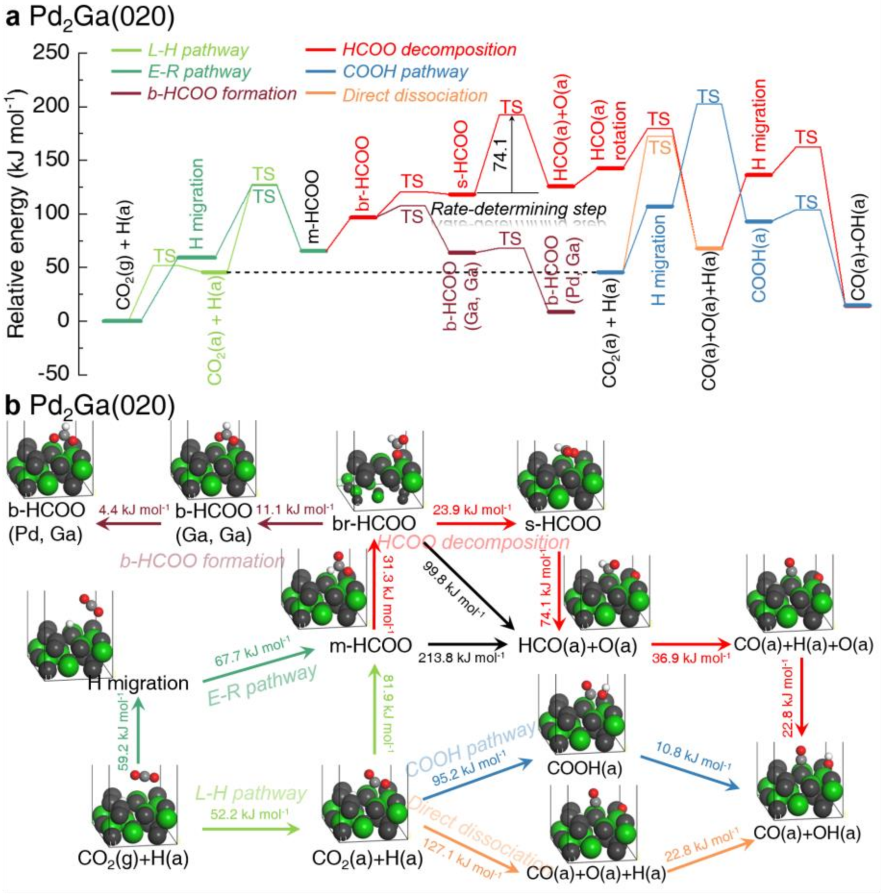

Figure 2.19. DFT calculations of the CO_2 hydrogenation reactions on $Pd_2Ga(020)$. (a) Energy diagram. (b) Corresponding DFT optimized geometries, showing the energy barriers. Color scheme: black, palladium; green, gallium; gray, carbon; red, oxygen; and white, hydrogen.

2.4.6 Reaction mechanisms of the CO_2 hydrogenation under NTP conditions

Figure 2.20 summarizes the mechanism of CO_2 hydrogenation over Pd_2Ga/SiO_2 under NTP conditions. The vibrationally-excited CO_2 promoted by plasma reacts directly with H atoms on the Pd site via the E−R pathway. Subsequently, the O atom is adsorbed to the Ga site eventually forming m-HCOO. As a subsequent step, H atoms adsorbed on the Pd site spillover to the Ga sites, and m-HCOO is decomposed into CO. The rate of formation and decomposition of m-HCOO is accelerated by NTP. As the hydrogen coverage has a shortage on the surface, the formation of CO is suppressed and part of m-HCOO is converted to b-HCOO. At this point, b- HCOO is quite stable. Under the NTP conditions, the decomposition of m-HCOO is further highlighted with sufficient H coverage on the surface. Other than the Pd_2Ga intermetallic phase, a small amount of monometallic Pd and Ga oxide is present. Although the interfacial sites of them might also be active for the NTP-assisted RWGS reaction, the contribution to the overall reaction rate should be minor because of the limited number of the Pd−Ga interface compared with that of intermetallic Pd_2Ga.

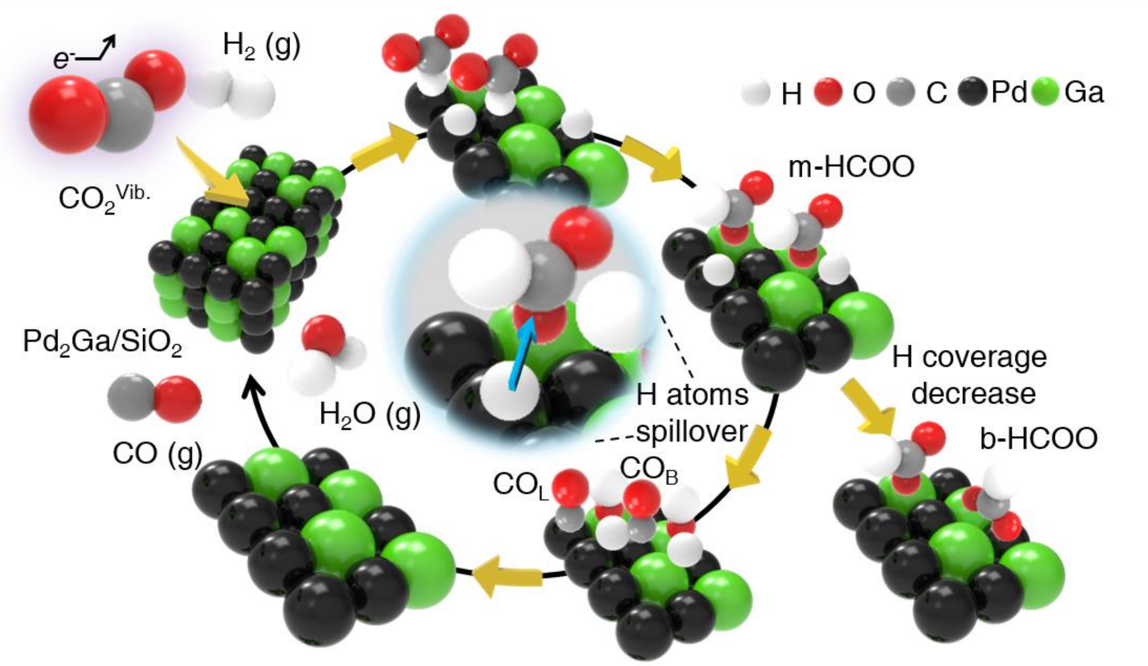

Figure 2.20. Proposed reaction mechanism of the CO_2 hydrogenation. Schematic illustration showing the CO_2 hydrogenation over the Pd_2Ga/SiO_2 by the vibrationally-excited CO_2 under NTP conditions via the E−R pathway.

2.5 Conclusions

In summary, I have shown that compared with the conventional thermal catalyst, the NTP-combined Pd_2Ga/ SiO_2 alloy catalyst system significantly improve CO_2 hydrogenation. More precisely, I elucidated that the bending mode of vibrationally-excited CO_2 species derived from NTP could lower the energy barrier and react with hydrogen atoms adsorbed on Pd sites via the E−R pathway and then accelerate formate formation due to the strong oxyphilic nature of Ga sites. The coupled experimental−theoretical study highlights that the combination of alloy catalysts and NTP is the key to promoting CO_2 hydrogenation and thereby could be beyond the thermodynamic limitation that is impossible to achieve with thermal catalysis. Our results demonstrated the reaction mechanism of fast formation and decomposition of m-HCOO for CO_2 hydrogenation over Pd_2Ga/SiO_2 alloy catalysts, implying that not only CO_2 activation but also H_2 activation is necessary for the enhanced spillover. Moreover, *in situ* XAFS results confirmed that a structural change of the alloyed catalyst and plasma heating effect are fully ruled out. The present study enables the high designability of CO_2 hydrogenation catalysts toward value-added chemicals based on the electrification of chemical processes via NTP.

2.6 References

1. S. Saeidi; Najari, S.; Hessel, V.; Wilson, K.; Keil, F. J.; Concepción, P.; Suib, S. L. & Rodrigues, A. E., Recent advances in CO_2 hydrogenation to value-added products—Current challenges and future directions, *Prog. Energy Combust. Sci.*, **85**, 100905 (2021).
2. D. Ravikumar; Zhang, D.; Keoleian, G.; Miller, S.; Sick, V. & Li, V., Carbon dioxide utilization in concrete curing or mixing might not produce a net climate benefit, *Nat. Commun.*, **12**, 1-13 (2021).
3. M. Bui, et al., Carbon capture and storage (CCS): the way forward, *Energy Environ. Sci.*, **11**, 1062-1176 (2018).
4. T. S. Galhardo; Braga, A. H.; Arpini, B. H.; Szanyi, J.; Gonçalves, R. V.; Zornio, B. F.; Miranda, C. R. & Rossi, L. M., Optimizing Active Sites for High CO Selectivity during CO_2 Hydrogenation over Supported Nickel Catalysts, *J. Am. Chem. Soc.*, **143**, 4268-4280 (2021).
5. N. Czaplicka; Konopacka-Łyskawa, D.; Kościelska, B. & Łapiński, M., Effect of selected ammonia escape inhibitors on carbon dioxide capture and utilization via calcium carbonate precipitation, *J. CO_2 Util.*, **42**, 101298 (2020).
6. M. Aresta; Dibenedetto, A. & Angelini, A., Catalysis for the valorization of exhaust carbon: from CO_2 to chemicals, materials, and fuels. Technological use of CO_2, *Chem. Rev.*, **114**, 1709-1742 (2014).
7. J. Bao; Yang, G.; Yoneyama, Y. & Tsubaki, N., Significant advances in C1 catalysis: highly efficient catalysts and catalytic reactions, *ACS Catal.*, **9**, 3026-3053 (2019).
8. X. Jiang; Nie, X.; Guo, X.; Song, C. & Chen, J. G., Recent advances in carbon dioxide hydrogenation to methanol via heterogeneous catalysis, *Chem. Rev.*, **120**, 7984-8034 (2020).
9. J. Zhong; Yang, X.; Wu, Z.; Liang, B.; Huang, Y. & Zhang, T., State of the art and

perspectives in heterogeneous catalysis of CO 2 hydrogenation to methanol, *Chem. Soc. Rev.*, **49**, 1385-1413 (2020).

10. C. Rameshan, et al., In situ XPS study of methanol reforming on PdGa near-surface intermetallic phases, *J. Catal.*, **290**, 126-137 (2012).

11. F. Studt; Sharafutdinov, I.; Abild-Pedersen, F.; Elkjær, C. F.; Hummelshøj, J. S.; Dahl, S.; Chorkendorff, I. & Nørskov, J. K., Discovery of a Ni-Ga catalyst for carbon dioxide reduction to methanol, *Nat. Chem.*, **6**, 320-324 (2014).

12. K. Mori; Sano, T.; Kobayashi, H. & Yamashita, H., Surface engineering of a supported PdAg catalyst for hydrogenation of CO_2 to formic acid: elucidating the active Pd atoms in alloy nanoparticles, *J. Am. Chem. Soc.*, **140**, 8902-8909 (2018).

13. X. Nie; Jiang, X.; Wang, H.; Luo, W.; Janik, M. J.; Chen, Y.; Guo, X. & Song, C., Mechanistic understanding of alloy effect and water promotion for Pd-Cu bimetallic catalysts in CO_2 hydrogenation to methanol, *ACS Catal.*, **8**, 4873-4892 (2018).

14. A. Bogaerts, et al., The 2020 plasma catalysis roadmap, *J. Phys. D: Appl. Phys.*, **53**, 443001 (2020).

15. Z. Sheng; Watanabe, Y.; Kim, H.-H.; Yao, S. & Nozaki, T., Plasma-enabled mode-selective activation of CH_4 for dry reforming: first touch on the kinetic analysis, *Chem. Eng. J.*, **399**, 125751 (2020).

16. S. Xu, et al., Mechanistic study of non-thermal plasma assisted CO_2 hydrogenation over Ru supported on MgAl layered double hydroxide, *Appl. Catal. B: Environ*, **268**, 118752 (2020).

17. S. Xu; Chansai, S.; Xu, S.; Stere, C. E.; Jiao, Y.; Yang, S.; Hardacre, C. & Fan, X., CO Poisoning of Ru Catalysts in CO_2 Hydrogenation under Thermal and Plasma Conditions: A Combined Kinetic and Diffuse Reflectance Infrared Fourier Transform Spectroscopy–Mass Spectrometry Study, *ACS Catal.*, **10**, 12828-12840 (2020).

18. H.-H. Kim, et al., Interim report of plasma catalysis: Footprints in the past and

blueprints for the future, *Int. J. Plasma Environ. Sci. Technol.*, **15**, e01004 (2021).

19. Z. Sheng; Kim, H.-H.; Yao, S. & Nozaki, T., Plasma-chemical promotion of catalysis for CH_4 dry reforming: unveiling plasma-enabled reaction mechanisms, *Phys. Chem. Chem. Phys.*, **22**, 19349-19358 (2020).

20. P. Destro; Kokumai, T. M.; Scarpellini, A.; Pasquale, L.; Manna, L.; Colombo, M. & Zanchet, D., The crucial role of the support in the transformations of bimetallic nanoparticles and catalytic performance, *ACS Catal.*, **8**, 1031-1037 (2018).

21. X. Zhang, et al., Reversible loss of core–shell structure for Ni–Au bimetallic nanoparticles during CO2 hydrogenation, *Nat. Catal.*, **3**, 411-417 (2020).

22. W. Zhan, et al., Crystal structural effect of AuCu alloy nanoparticles on catalytic CO oxidation, *J. Am. Chem. Soc.*, **139**, 8846-8854 (2017).

23. J. Quan; Kondo, T.; Wang, G. & Nakamura, J., Energy transfer dynamics of formate decomposition on Cu(110), *Angew. Chem. Int. Ed.*, **129**, 3550-3554 (2017).

24. J. Quan, et al., Vibration-driven reaction of CO_2 on Cu surfaces via Eley–Rideal-type mechanism, *Nat. Chem.*, **11**, 722-729 (2019).

25. J. Yu; Yang, M.; Zhang, J.; Ge, Q.; Zimina, A.; Pruessmann, T.; Zheng, L.; Grunwaldt, J.-D. & Sun, J., Stabilizing Cu+ in Cu/SiO2 catalysts with a shattuckite-like structure boosts CO2 hydrogenation into methanol, *ACS Catal.*, **10**, 14694-14706 (2020).

26. S. E. Collins; Baltanás, M. A.; Delgado, J. J.; Borgna, A. & Bonivardi, A. L., CO2 hydrogenation to methanol on Ga2O3-Pd/SiO2 catalysts: Dual oxide-metal sites or (bi) metallic surface sites?, *Catal. Today*, **381**, 154-162 (2021).

27. K. Feng; Tian, J.; Guo, M.; Wang, Y.; Wang, S.; Wu, Z.; Zhang, J.; He, L. & Yan, B., Experimentally unveiling the origin of tunable selectivity for CO2 hydrogenation over Ni-based catalysts, *Appl. Catal. B: Environ*, **292**, 120191 (2021).

28. C. Schild; Wokaun, A.; Koeppel, R. A. & Baiker, A., Carbon dioxide hydrogenation over nickel/zirconia catalysts from amorphous precursors: on the mechanism of

methane formation, *J. phys. chem.*, **95**, 6341-6346 (1991).

29. L. F. Bobadilla; Santos, J. L.; Ivanova, S.; Odriozola, J. A. & Urakawa, A., Unravelling the role of oxygen vacancies in the mechanism of the reverse water–gas shift reaction by operando DRIFTS and ultraviolet–visible spectroscopy, *ACS Catal.*, **8**, 7455-7467 (2018).

30. A. M. Bahmanpour; Signorile, M. & Kröcher, O., Recent progress in syngas production via catalytic CO2 hydrogenation reaction, *Appl. Catal. B: Environ*, 120319 (2021).

31. S. Xu; Chen, H.; Hardacre, C. & Fan, X., Non-thermal plasma catalysis for CO_2 conversion and catalyst design for the process, *J. Phys. D: Appl. Phys.*, **54**, 233001 (2021).

32. P. Mehta; Barboun, P.; Herrera, F. A.; Kim, J.; Rumbach, P.; Go, D. B.; Hicks, J. C. & Schneider, W. F., Overcoming ammonia synthesis scaling relations with plasma-enabled catalysis, *Nat. Catal.*, **1**, 269-275 (2018).

33. S. Xu, et al., Sustaining metal–organic frameworks for water–gas shift catalysis by non-thermal plasma, *Nat. Catal.*, **2**, 142-148 (2019).

34. E. M. Fiordaliso; Sharafutdinov, I.; Carvalho, H. W.; Grunwaldt, J.-D.; Hansen, T. W.; Chorkendorff, I.; Wagner, J. B. & Damsgaard, C. D., Intermetallic GaPd2 nanoparticles on SiO2 for low-pressure CO2 hydrogenation to methanol: Catalytic performance and in situ characterization, *ACS Catal.*, **5**, 5827-5836 (2015).

35. A. s. García-Trenco; White, E. R.; Regoutz, A.; Payne, D. J.; Shaffer, M. S. & Williams, C. K., Pd2Ga-based colloids as highly active catalysts for the hydrogenation of CO2 to methanol, *ACS Catal.*, **7**, 1186-1196 (2017).

36. J. Madarász; Bombicz, P.; Mátyás, C.; Réti, F.; Kiss, G. & Pokol, G., Comparative evolved gas analytical and structural study on trans-diammine-bis (nitrito)-palladium (II) and platinum (II) by TG/DTA–MS, TG–FTIR, and single crystal X-ray diffraction, *Thermochim. Acta*, **490**, 51-59 (2009).

37. S. Kameshima; Tamura, K.; Ishibashi, Y. & Nozaki, T., Pulsed dry methane reforming in plasma-enhanced catalytic reaction, *Catal. Today*, **256**, 67-75 (2015).

38. S. Kameshima; Tamura, K.; Mizukami, R.; Yamazaki, T. & Nozaki, T., Parametric analysis of plasma-assisted pulsed dry methane reforming over Ni/Al_2O_3 catalyst, *Plasma Process. Polym.*, **14**, 1600096 (2017).

39. S. Kameshima; Mizukami, R.; Yamazaki, T.; Prananto, L. A. & Nozaki, T., Interfacial reactions between DBD and porous catalyst in dry methane reforming, *J. Phys. D: Appl. Phys.*, **51**, 114006 (2018).

40. Z. Sheng; Sakata, K.; Watanabe, Y.; Kameshima, S.; Kim, H.-H.; Yao, S. & Nozaki, T., Factors determining synergism in plasma catalysis of biogas at reduced pressure, *J. Phys. D: Appl. Phys.*, **52**, 414002 (2019).

41. K. K. Lee; Han, G. Y.; Yoon, K. J. & Lee, B. K., Thermocatalytic hydrogen production from the methane in a fluidized bed with activated carbon catalyst, *Catal. Today*, **93**, 81-86 (2004).

42. A. Gómez-Barea; Ollero, P. & Leckner, B., Mass transport effects during measurements of gas–solid reaction kinetics in a fluidised bed, *Chem. Eng. Sci.*, **62**, 1477-1493 (2007).

43. A. L. Ankudinov; Ravel, B.; Rehr, J. & Conradson, S., Real-space multiple-scattering calculation and interpretation of x-ray-absorption near-edge structure, *Phys. Rev. B*, **58**, 7565 (1998).

44. M. Segall; Lindan, P. J.; Probert, M. a.; Pickard, C. J.; Hasnip, P. J.; Clark, S. & Payne, M., First-principles simulation: ideas, illustrations and the CASTEP code, *J. Phys.: Condens. Matter*, **14**, 2717 (2002).

45. B. Hammer; Hansen, L. B. & Nørskov, J. K., Improved adsorption energetics within density-functional theory using revised Perdew-Burke-Ernzerhof functionals, *Phys. Rev. B: Condens. Matter Mater. Phys.*, **59**, 7413 (1999).

46. Y. Zhang & Yang, W., Comment on “Generalized gradient approximation made simple”,

Phys. Rev. Lett., **80**, 890 (1998).

47. A. Tkatchenko & Scheffler, M., Accurate molecular van der Waals interactions from ground-state electron density and free-atom reference data, *Phys. Rev. Lett.*, **102**, 073005 (2009).

48. H. J. Monkhorst & Pack, J. D., Special points for Brillouin-zone integrations, *Phys. Rev. B*, **13**, 5188 (1976).

49. N. Govind; Petersen, M.; Fitzgerald, G.; King-Smith, D. & Andzelm, J., A generalized synchronous transit method for transition state location, *Comput. Mater. Sci.*, **28**, 250-258 (2003).

50. T. A. Halgren & Lipscomb, W. N., The synchronous-transit method for determining reaction pathways and locating molecular transition states, *Chem. Phys. Lett.*, **49**, 225-232 (1977).

51. X. Chen; Sheng, Z.; Murata, S.; Zen, S.; Kim, H.-H. & Nozaki, T., CH4 dry reforming in fluidized-bed plasma reactor enabling enhanced plasma-catalyst coupling, *J. CO_2 Util.*, **54**, 101771 (2021).

52. F. Gao; Wang, Y. & Goodman, D. W., CO oxidation over AuPd(100) from ultrahigh vacuum to near-atmospheric pressures: the critical role of contiguous Pd atoms, *J. Am. Chem. Soc.*, **131**, 5734-5735 (2009).

53. H. Jeong; Bae, J.; Han, J. W. & Lee, H., Promoting effects of hydrothermal treatment on the activity and durability of Pd/CeO_2 catalysts for CO oxidation, *ACS Catal.*, **7**, 7097-7105 (2017).

54. H. Xu, et al., Entropy-stabilized single-atom Pd catalysts via high-entropy fluorite oxide supports, *Nat. Commun.*, **11**, 1-9 (2020).

55. H. Jeong; Kwon, O.; Kim, B.-S.; Bae, J.; Shin, S.; Kim, H.-E.; Kim, J. & Lee, H., Highly durable metal ensemble catalysts with full dispersion for automotive applications beyond single-atom catalysts, *Nat. Catal.*, **3**, 368-375 (2020).

56. S. E. Collins; Chiavassa, D. L.; Bonivardi, A. L. & Baltanas, M. A., Hydrogen spillover in Ga_2O_3–Pd/SiO_2 catalysts for methanol synthesis from CO_2/H_2, *Catal. Lett.*, **103**, 83-88 (2005).

57. Y. Wang, et al., Ensemble effect in bimetallic electrocatalysts for CO_2 reduction, *J. Am. Chem. Soc.*, **141**, 16635-16642 (2019).

58. R. Manrique; Jiménez, R.; Rodríguez-Pereira, J.; Baldovino-Medrano, V. G. & Karelovic, A., Insights into the role of Zn and Ga in the hydrogenation of CO_2 to methanol over Pd, *Int. J. Hydrogen Energy*, **44**, 16526-16536 (2019).

59. G. C. Cabilla; Bonivardi, A. L. & Baltanás, M. A., Characterization by CO/FTIR spectroscopy of Pd/silica catalysts and its correlation with syn-gas conversion, *Catal. Lett.*, **55**, 147-156 (1998).

60. G. Spezzati; Su, Y.; Hofmann, J. P.; Benavidez, A. D.; DeLaRiva, A. T.; McCabe, J.; Datye, A. K. & Hensen, E. J., Atomically dispersed Pd–O species on CeO_2 (111) as highly active sites for low-temperature CO oxidation, *ACS Catal.*, **7**, 6887-6891 (2017).

61. S. R. Docherty; Phongprueksathat, N.; Lam, E.; Noh, G.; Safonova, O. V.; Urakawa, A. & Copéret, C., Silica-supported PdGa Nanoparticles: Metal Synergy for Highly Active and Selective CO_2-to-CH_3OH Hydrogenation, *JACS Au*, **1**, 450-458 (2021).

62. E. C. Neyts; Ostrikov, K.; Sunkara, M. K. & Bogaerts, A., Plasma catalysis: synergistic effects at the nanoscale, *Chem. Rev.*, **115**, 13408-13446 (2015).

63. H. Nakano; Nakamura, I.; Fujitani, T. & Nakamura, J., Structure-dependent kinetics for synthesis and decomposition of formate species over Cu(111) and Cu(110) model catalysts, *J. phys. chem. B*, **105**, 1355-1365 (2001).

64. Y. Yang; Mims, C. A.; Disselkamp, R. S.; Mei, D.; Kwak, J.-H.; Szanyi, J.; Peden, C. H. & Campbell, C., Isotope Effects in Methanol Synthesis and the Reactivity of Copper Formates on a Cu/SiO_2 Catalyst, *Catal. Lett.*, **125**, 201-208 (2008).

65. Y. Yang; Mims, C. A.; Disselkamp, R. S.; Kwak, J.-H.; Peden, C. H. & Campbell, C.,

(Non) formation of methanol by direct hydrogenation of formate on copper catalysts, *J. phys. chem. C*, **114**, 17205-17211 (2010).

66. L. Falbo; Visconti, C. G.; Lietti, L. & Szanyi, J., The effect of CO on CO_2 methanation over Ru/Al_2O_3 catalysts: a combined steady-state reactivity and transient DRIFT spectroscopy study, *Appl. Catal. B: Environ*, **256**, 117791 (2019).

67. X. Wang; Hong, Y.; Shi, H. & Szanyi, J., Kinetic modeling and transient DRIFTS–MS studies of CO_2 methanation over Ru/Al_2O_3 catalysts, *J. Catal.*, **343**, 185-195 (2016).

68. X. Yang, et al., Promotion effects of potassium on the activity and selectivity of Pt/zeolite catalysts for reverse water gas shift reaction, *Appl. Catal. B: Environ*, **216**, 95-105 (2017).

69. A. Walsh, The electronic orbitals, shapes, and spectra of polyatomic molecules. Part II. Non-hydride AB_2 and BAC molecules, *J. Chem. Soc.*, 2266-2288 (1953).

70. M. B. Ansari & Park, S.-E., Carbon dioxide utilization as a soft oxidant and promoter in catalysis, *Energy Environ. Sci.*, **5**, 9419-9437 (2012).

71. R. Snoeckx & Bogaerts, A., Plasma technology–a novel solution for CO_2 conversion?, *Chem. Soc. Rev.*, **46**, 5805-5863 (2017).

72. E. K. Gibson, et al., Probing the role of a non-thermal plasma (NTP) in the hybrid NTP catalytic oxidation of methane, *Angew. Chem. Int. Ed.*, **56**, 9351-9355 (2017).

73. S. Gowtham; Deshpande, M.; Costales, A. & Pandey, R., Structural, energetic, electronic, bonding, and vibrational properties of Ga_3O, Ga_3O_2, Ga_3O_3, Ga_2O_3, and GaO_3 clusters, *J. phys. chem. B*, **109**, 14836-14844 (2005).

74. A. M. Appel, et al., Frontiers, opportunities, and challenges in biochemical and chemical catalysis of CO_2 fixation, *Chem. Rev.*, **113**, 6621-6658 (2013).

Chapter 3. *In situ* infrared absorption probing of plasma catalysis: vibrationally-excited species induced Mars−van Krevelen type mechanism

The content of this chapter has been published in *Plasma. Sources. Sci. Technol.* [Kim. DY. et al *Plasma. Sources. Sci. Technol* 31, 124005 (2022).]

3.1 Abstract

Nonthermal plasma (NTP) assisted catalysis has recently received attention as an attractive technology that can overcome the energy barriers involved in conventional thermal catalysis. It is important to obtain fundamental insight into the synergistic effects arising from interactions between NTP-activated species and catalysis. However, it remains a challenge due to difficulties associated with the *in situ* characterization of NTP-activated species. In this study, CO was explored in dielectric barrier discharge by applying *in situ* transmission infrared (TIR) absorption spectroscopy; TIR enables the measurement of the vibrational temperature of CO while observing the surface reaction of excited CO to form intermediates species over wurtzite ZnO. The reaction behavior of activated CO correlates with the vibrational temperature of CO, showing vibrationally-excited CO reacts with lattice oxygen via the Mars–van Krevelen mechanism; thus, leading to higher activity compared with conventional thermal catalysis. This work helps to understand the fundamental chemistry and provides new insight into NTP-activated CO and its catalysis.

3.2 Introduction

Nonthermal plasma (NTP) assisted catalysis, which combines NTP and heterogenous catalysts, has been attracting attention as an alternative to conventional thermal catalysis in various environmental and energy fields[1-10]. NTP is characterized by having abundant vibrationally-excited molecules with various active species including ions, radicals, and free electrons which arise due to inelastic collisions between high-energy electrons and ground-state molecules[11-13]. NTP-assisted catalysis generates activated species that are inaccessible at bulk thermal temperatures. This effectively makes thermodynamically challenging reaction possible by removing the thermal equilibrium limitations experienced in conventional catalysis[14]. Although the synergistic effects in NTP-assisted catalysis are elicited by the rational design of catalysts, they depend on a fundamental understanding of the surface activity and reaction mechanisms relationships at the molecular level.

In the NTP environment, vibrationally-excited molecules are dominant channels because of their low energy threshold compared with ionization or dissociation[15]. This point is particularly important as unique reaction pathways arise[15-19]. However, the lack of direct spectral evidence for vibrationally-excited molecules for catalysis is controversial and the reaction mechanism of NTP-assisted catalysis is poorly understood. As the elucidation of interactions between the catalytic surfaces and NTP-active species is challenging, it is essential to develop spectroscopic techniques that enable the *in situ* analysis of the catalytic surface reaction in the NTP environment. *In situ* Fourier transform infrared spectroscopy (FTIR) is one of the most powerful spectroscopic techniques to investigate the reaction mechanism through *in situ* monitoring of catalytic surface reactions[20-22] and to gain insight into the vibrationally-excited state of molecules[23-25].

The interactions at the catalytic surface of gas molecules (reactants) generally follow three well-established mechanisms: Langmuir–Hinshelwood (L–H), Eley–Rideal (E–R) and Mars–van Krevelen (MvK) mechanisms. Previously reported NTP-assisted catalysis studies have reported that vibrationally-excited and dissociation species activated by NTP can promote catalytic reactions via E–R and/or L–H type mechanisms[8,14,16,26,27]. In contrast, thus far, there have been no reports of MvK type mechanisms in NTP-assisted catalysis. ZnO is considered a major component in various catalytic processes[28-30]. In particular, the catalytic surface chemistry of CO over ZnO can be oxidized via the MvK mechanism[31-33]; CO molecules adsorbed at Zn ions directly react with adjacent lattice oxygen atoms to form CO_2 and oxygen vacancies (R3.1). The oxygen vacancies are then healed by. Gas phase O_2 (R3.2)

$$CO + ZnO \rightarrow CO_2 + ZnO_{1-x} \qquad \text{R3.1}$$

$$O_2 + ZnO_{1-x} \rightarrow ZnO + O \qquad \text{R3.2}$$

The reducibility of ZnO is an essential property of oxidation reactions and is of interest to researchers in the field of catalysis[32-35]. A typical descriptor of this reducibility is the formation of oxygen vacancies, which can be measured by the observation of adsorbed species, along with the resulting change in the surface composition[34]. However, the process in (1) above is generally endothermic and at low temperatures may be unfavorable[33,36,37].

Herein, I compare the catalysis of NTP-activated CO with the conventional thermal catalysis over wurtzite ZnO. By applying *in situ* transmission infrared (TIR) absorption spectroscopy, where the catalytic surface can be identified during dielectric barrier discharge (DBD) irradiation, the detection of the IR-activated vibrationally-excited CO and their catalytic surface evolution was directly correlated at room temperature (ca. 300 K). I found that in the DBD conditions, the rotational temperature of CO remained close to room temperature, while the vibrational temperature increased by higher than 1000 K. Furthermore, the density of the vibrationally-excited CO species was controlled by the DBD power. These insights eliminated the effect of gas heating by DBD and allowed us to quantitatively confirm the surface reaction channels of vibrationally-excited CO over ZnO. From the observation of the catalytic surface reaction of the ZnO through *in situ* TIR, ZnO remains inert with CO in the ground-state at room temperature, whereas CO oxidation is promoted under DBD conditions to promote the formation of carbonate. Through this study, I report that DBD-activated vibrationally-excited CO promotes thermodynamically limited CO oxidation via the MvK type mechanism.

3.3 Experiment section

3.3.1 Material and Characterization

CO activation was performed over commercial ZnO powder (Kanto Chemical Co. Inc). The experiments were performed with a CO-Ar mixture (10 % CO by volume) and the Ar. ZnO powder was characterized by X-ray diffraction (XRD) measurements. The XRD of ZnO powder was performed on a Rigaku SmartLab diffractometer, using a Cu Kα radiation source ($\lambda = 0.15418$ nm). The diffraction patterns to the wurtzite ZnO structure were observed (Figure 3.1).

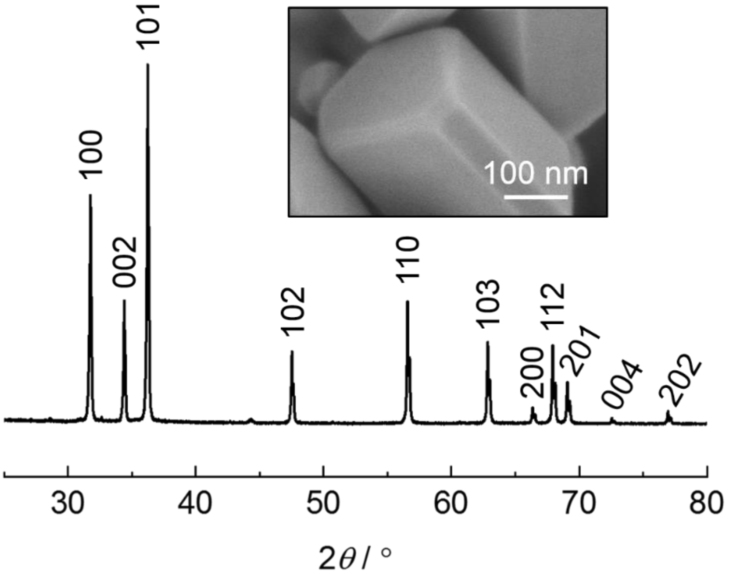

Figure 3.1. XRD patterns of ZnO. The inset shows the SEM image of ZnO, indicating it is hexagonal.

3.3.2 *In situ* TIR

In situ TIR absorption spectroscopy over ZnO pellet was performed using an IR reactor equipped with a DBD system (Figure 3.2) under a pressure of 5 kPa. The reactor was composed of quartz glass with an inner diameter of 25 mm, and the path length was 11.6 cm. ZnSe windows were set on both ends of the reactor. Stainless steel (1 mm o.d.) high voltage and ground electrodes were inserted inside the reactor center. The high voltage electrode was wrapped with an alumina tube and only the metal tip was exposed to the gas flow, while the grounded electrode was fully covered by a quartz sheath. A K-type thermocouple (1 mm o.d.) was arranged at the 12 o'clock position above the high voltage and ground electrodes to detect the temperature inside the reactor (Figure 3.2c). The electrical parameters were monitored using an oscilloscope (RIGOL MSO5104) connected to the reactor via a high voltage probe. The gap between the point-to-point electrodes was 10 mm. A high voltage power supply was connected to the reactor and the applied power was 0.058, 0.066, and 0.078 W.

To prepare the ZnO powder (ca. 50 mg) in the form of a pellet (10 mm o.d., 1 mm thickness), the powder was uniformly transferred to a disk kit and compressed at ca. 1.5 MPa. Thereafter, the catalyst was fixed in a glass holder and inserted into the TIR reactor. The TIR spectra were measured using a JASCO FTIR-6600 spectrometer equipped with a mercury−cadmium−telluride (MCT) detector with a spectral resolution of 4 cm^{-1}. Prior to the IR absorption spectroscopic experiments, the ZnO pellet was treated with H_2 (flow rate, 3 cm^3 min^{-1}) and Ar (flow rate, 40 cm^3 min^{-1}) at ca. 770 K for 1 h. The pellet was subsequently cooled to room temperature in an Ar atmosphere and the background spectra were obtained. For CO activation experiments, the CO and Ar mixture was introduced at 5 kPa (flow rate, CO = 1 cm^3 min^{-1} and Ar = 49 cm^3 min^{-1}).

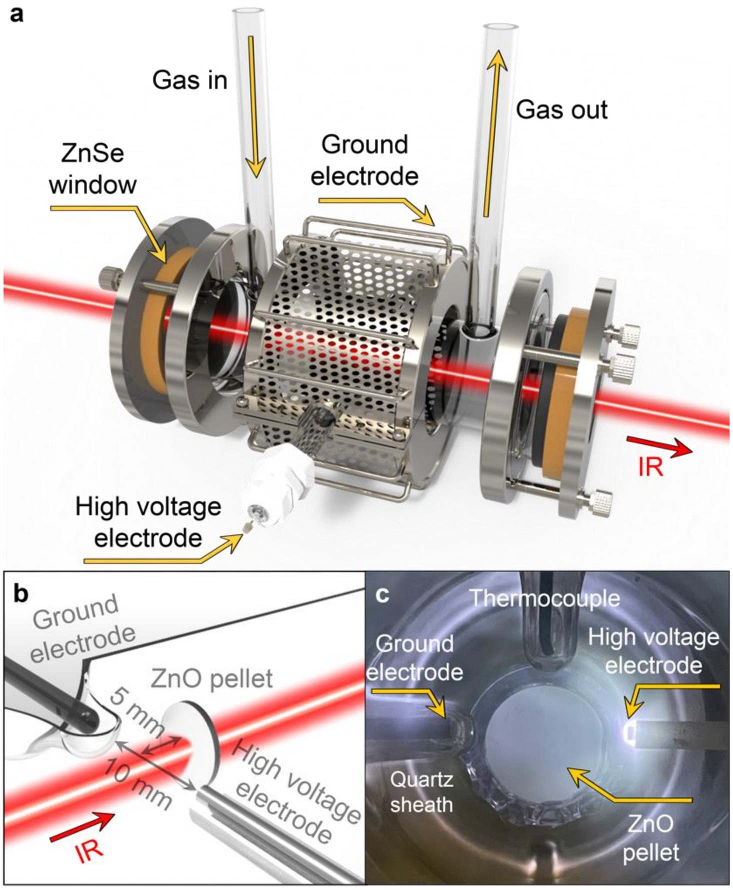

Figure 3.2. (a) 3D Schematic illustration of *in situ* TIR DBD reactor which is capable of identifying catalytic surface species with and without DBD irradiation. Gas-phase IR absorption spectroscopy is also possible using blank TIR reactor (without catalyst pellet). (b) 3D schematic diagram electrodes and ZnO pellet geometry. (c) Photograph emission from DBD (0.058W).

3.4 Result and discussion

3.4.1 Measurement of vibrational temperature

First, I performed *in situ* TIR in 2 % CO in Ar steam at 5 kPa in a blank (without catalyst) TIR reactor at room temperature (ca. 300 K) to gain insight into vibrationally-excited CO species under DBD conditions (Figure 3.3a). At this time, the spectral resolution was set to 0.5 cm^{-1}. An increase in absorbance can be clearly observed at the lower wavenumber band resulting from the transition of the quantum number of vibrationally-excited CO ($\nu_{\mathrm{co}} = 1 \rightarrow 2$) under a DBD power of 0.058 W. The vibrational temperature (T_{vib}) of CO was estimated from the modeled optimal spectra using a fast line-by-line code RADIS[38] assuming a Boltzmann distribution of vibrational energy. As shown in Figure 3.3b, the best fit of DBD power of 0.058 W at 5 kPa under a 2 % CO in Ar stream is obtained with a rotational temperature (T_{rot}) = 300 ± 10 K and $T_{\mathrm{vib}} = 1000 \pm 100$ K. The temperature of the vibrationally-excited CO was further investigated for higher DBD power of 0.066 and 0.078 W (Figure 3.3c). T_{rot} remains close to room temperature while T_{vib} increases with the DBD power developing toward 1300 K at 0.078 W. The DBD power dependence on T_{rot} is weak. This is explained by the low excitation efficiency of the rotational degree of freedom because the transfer of momentum from high-energy electrons to the ground-state molecules is limited due to the conservation of angular momentum[39]. I also measured the reactor temperature via a thermocouple, and a negligible temperature increase of ca. 10 K was observed under DBD conditions. Vibrationally-excited CO species can be efficiently induced via energy transfer from low energy electrons to the ground-state CO under the DBD conditions. Therefore, T_{rot} and T_{vib} are generally different in nonequilibrium excited molecules. When the anharmonicity of the diatomic molecules is large and the high vibrational temperature exceeds 3000 K, due to the strong nonequilibrium excitation of the molecules, the vibrational-vibrational process is non-resonant[15,40]. Due to this occurrence, the population of the high-vibration states has a large deviation from the Boltzmann distribution[41,42]. Thus, a non-resonant vibrational-vibrational process should be considered through the Treanor distribution. However, the population of the first few vibrational states has a small anharmonicity, so the vibrational-vibrational process can resonate. Therefore, the deviation of the Boltzmann distribution can be kept below the sensitivity limit. I assumed the Boltzmann distribution for the weak nonequilibrium discharge condition applied in this work and showed good fitting results as shown in Figure 3.3b. Moreover, at the measured low vibrational temperature of approximately 1000−1300 K, the population in the high vibration state is very low, so it cannot be evaluated with the Treanor distribution because of the non-resonant vibrational-vibrational process[40]. From theses insight, I can rule out the effects on ionization and ions. Moreover, the first excited electronic state, CO($a^3\Pi$), can be ruled out due to its high potential energy of 6.006 eV, which is nearly isoenergetic at high vibrational levels above 26[43]. That is, our DBD system can selectively activate the vibrational excitation mode of CO molecules.

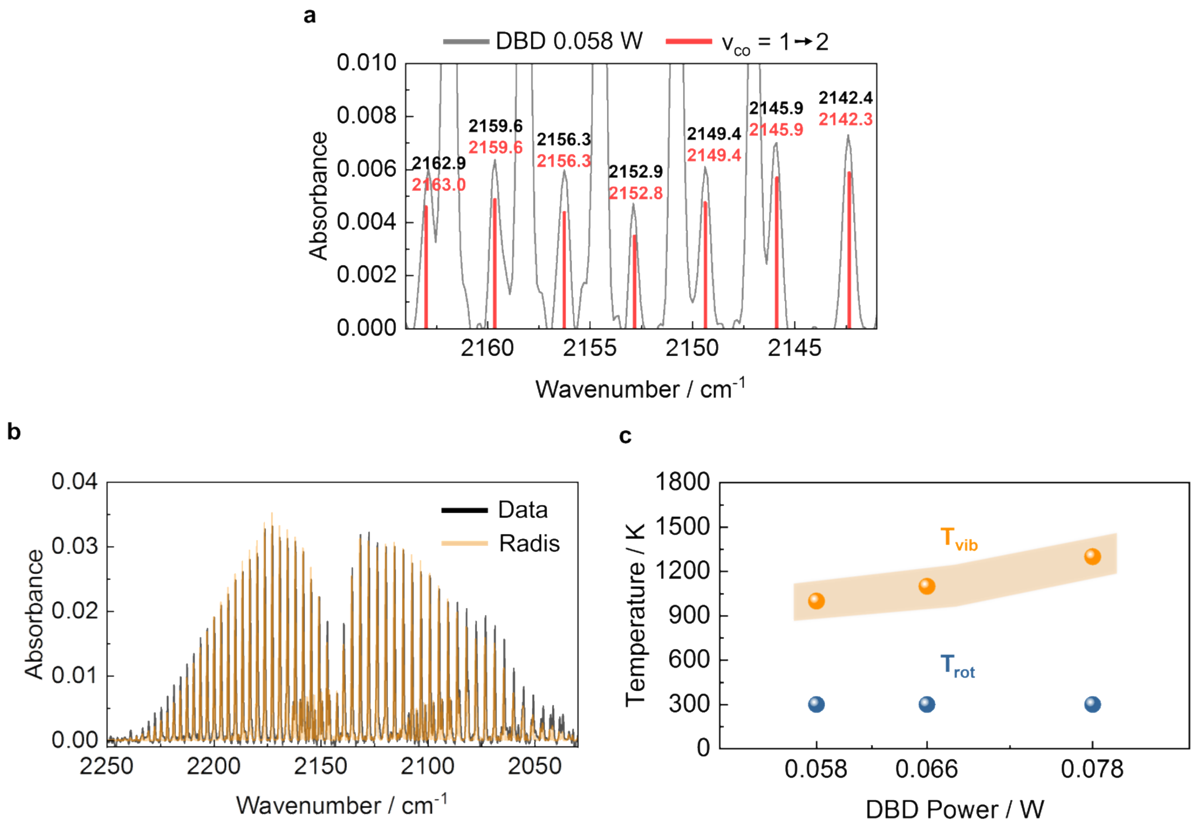

Figure 3.3. (a) Vibrationally-excited CO TIR spectra taken at DBD power of 0.058 W at 2 % CO in Ar (50 cm^3 min^{-1}) stream at room temperature. (b) Comparison between simulated and experimental CO TIR spectra at same conditions with (a). (c) Rotational and vibrational temperatures measured at DBD power of 0.058, 0.066, and 0.078 W at 2 % CO in Ar stream.

3.4.2 Population quantification of vibrationally-excited CO

The population quantification of vibrationally-excited CO provides useful information about the energy exchange processes occurring under DBD conditions. The density of the vibrationally excitation levels was predicted via a partition function assuming that the vibrational energy follows the Boltzmann distribution (Figure 3.4). The density of the vibrationally-excited CO shows the dependence on DBD power, and the population distribution of the main vibrationally-excited CO up to a quantum number of three. A higher DBD power results in either a high electron energy or electron number density; in both cases, a collision between electrons and CO would be enhanced and a higher vibrational temperature is possible. This makes DBD suitable for investigating the ZnO surface reaction channel supported by vibrationally-excited CO. Moreover, in our previous work, the temperature of nanometer-sized metallic components of catalyst was measured by *in situ* X-ray absorption fine-structure (XAFS), showing that a DBD-induced temperature increase was not confirmed[14]. Therefore, our DBD system excludes even the influence of unwanted surface reactions by heating the ZnO surface.

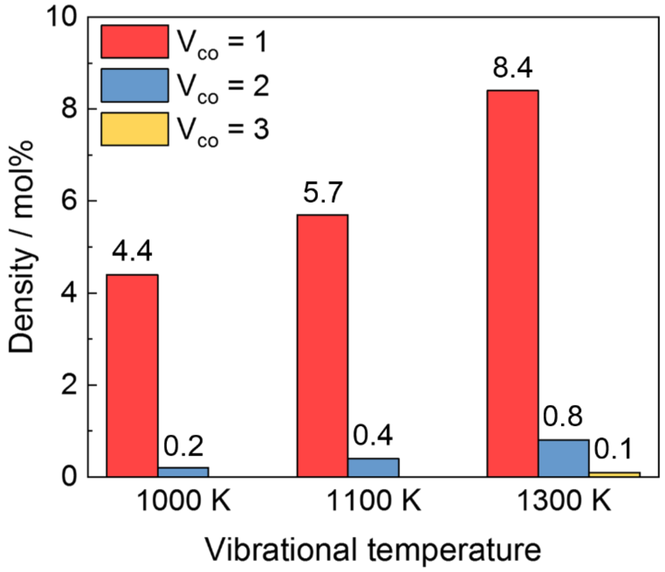

Figure 3.4. Density distribution of vibrationally-excited CO calculated at vibrational temperatures of 1000, 1100 and 1300 K while gas temperature is assumed to be constant at 300 K. Y-axis represents mol % of density of vibrationally-excited CO relative to total CO density.

3.4.3 Investigation of the surface response by vibrationally-excited CO

Subsequently, I discuss the *in situ* TIR spectra of the wurtzite ZnO surface response to vibrationally-excited CO and thereby the evolution of the surface species; I compared it with the surface reaction with ground-state CO. Figure 3.5 shows the temporal evolution of the spectra recorded during the reaction with ground-state CO (labeled as thermal) and vibrationally-excited CO (labeled as DBD). As shown in Figure 3.5a, it is difficult to identify a clear peak due to carbonate in the region of 1800 to 1200 cm^{-1} under thermal conditions. Moreover, in the CO-related spectral region of 2300 to 2000 cm^{-1}, a small peak at 2060 cm^{-1}, due to adsorbed CO, is observed in addition to the CO gas phase ($CO_{(g)}$). However, the 2060 cm^{-1} peak disappears when the CO flow is turned off. As a result, ground-state CO has a weak interaction with the ZnO surfaces. However, the reactivity of CO changes prominently under DBD conditions. When the ZnO surface is exposed to vibrationally-excited CO by a DBD power of 0.058 W, a sharp increase in the bands of adsorbed bicarbonate (HCO_3^*: 1635, 1411 and 1225 cm^{-1})[44,45] and carbonate (CO_3^*: 1514 and 1341 cm^{-1})[46] are detected. Bicarbonate is formed when the surface OH groups are consumed[47] (Figure 3.7).

When the surface OH. Groups are removed by strict pretreatment conditions; the formation of bicarbonate is suppressed (Figure 3.6). It has been demonstrated by previous theoretical and FTIR experiments studies that CO_2 produced through CO oxidation on the catalyst can react with the surface to from (bi)carbonate[48-52]. The. appearance of (bi)carbonate suggests that the oxidation of vibrationally-excited CO is responsible for the generation of intermediate species. Vibrationally-excited molecules have a higher energy level than the ground-state molecules corresponding with the vibrational energy. The internal vibrational energy can provide more reactivity by reducing or removing the activation barrier at the catalyst surface. Moreover, upon the chemisorption of the vibrationally-excited molecules on the catalyst surface, the catalyst surface can retain sufficient energy to supply endothermic energy[53]. The CO oxidation on the reducible metal oxides mainly occurs via the reaction of lattice oxygen species and CO, known as the MvK mechanism[31-34]. The experiments were performed at room temperature; therefore, ground-state CO does not react with the lattice oxygen of ZnO. At a relatively high temperature of 470 K, carbonate formation is observed under thermal conditions (Figure 3.6). Conversely, the evolution of the (bi)carbonate species observed even at room temperature under DBD conditions suggests that vibrationally-excited CO promotes a thermodynamically limited MvK type mechanism. This is further confirmed in the CO spectral region from 2300 to 2000 cm^{-1} (Figure 3.5b). The evolution of bands attributed to CO adsorption (CO^*) at 2106 and 2155 cm^{-1} was initiated in approximately 5 min. I can find a correlation between the immediate formation of carbonate and the appearance of a late CO adsorption band. The CO oxidation reaction by the MvK type mechanism is a reaction that forms oxygen vacancies. Therefore, to predict the activity of the catalytic CO oxidation, the formation energy of the oxygen vacancies is taken as the main indicator[34]. That is, the late evolution of the CO adsorption band suggests a decrease in the CO oxidation reaction rate by the formation of oxygen vacancies. This occurrence can be supported by a decrease in the formation rate of (bi)carbonate over time (e.g. Figure 3.8). It must be discussed further that the observed wavenumber at 2106 cm^{-1} is unexpectedly red-shifted, and the adsorbed CO on Zn^{2+} is generally characterized between 2200 to 2170 cm^{-1}[54,55]. Similar observations have been previously reported by Schott et al[56]. The authors report that a distorted ZnO, different from wurtzite ZnO, exhibits significant charge flow, and this chemical property increases the CO binding energy with Zn^{2+} and is accompanied by a red-shift of the CO adsorption band[56]. The CO adsorption band observed in this study did not disappear even after the CO flow was turned off (Figure 3.5b), confirming the high stability. This observation represents a reasonable agreement with the study of Schott et al. Therefore, I suggest that vibrationally-excited CO promotes adsorption on Zn^{2+} and is generally recognized as an active site for Zn, and subsequently reacts with adjacent lattice oxygen. Additionally, CO can more strongly adsorb to metal ions that are not shielded (or less shielded) by oxygen on the oxide surface[57-59]. That is, the CO adsorbed on Zn^{2+} observed under DBD conditions can be derived from the subsequent adsorption of ground-state CO to unshielded Zn^{2+} formed by the reaction with vibrationally-excited CO. Therefore, I investigated the behavior of the CO adsorption band by exposing the ZnO surface to CO for a specific time under DBD conditions and then switching to thermal conditions (Figure 3.5c). When the ZnO surface was exposed to vibrationally-excited CO with a DBD power of 0.058 W for 10 min, CO adsorption bands at 2155 and 2106 cm^{-1} are observed (yellow spectra at the top). Thereafter, when switched to ground-state CO (DBD off, black spectra), the CO adsorption band at 2155 and 2106 cm^{-1} gradually disappear, and when the CO gas is turned off after 10 min, no CO adsorption band is observed. These observations support the premise that the CO adsorption bands appearing under DBD conditions are due to the adsorption of vibrationally-excited CO to Zn^{2+}, and the effect of ground-state CO adsorption is excluded.

I further investigated the evolution of *in situ* TIR spectra for CO adsorption and (bi)carbonate formation on the ZnO surfaces at higher DBD powers. Figure 3.8a shows the spectra of the CO adsorption band recorded at 5 min after CO exposure under different DBD powers. At a DBD power of 0.058 W, the CO adsorption bands at 2106 and 2155 cm^{-1} are difficult to observe as they are not strong enough to distinguish from $CO_{(g)}$. However, from a DBD power of 0.066 W, CO adsorption bands distinguishable from $CO_{(g)}$ begin to appear and appear to increase further at 0.078 W. Figure 3.8b presents a two-dimensional plot of the normalized intensity versus the temporal evolution of carbonate (1514 cm^{-1}) formed on the surface. Of note is that at higher DBD power, higher density vibrationally-excited CO species are formed. As might be expected, carbonate formation on the surface of the ZnO further increases with DBD power. When the electrons are charged to ZnO, some of the electrons are donated to the ZnO conduction band and IR photons are absorbed due to interactions with bulk plasmons, resulting in an increase in the background absorbance signal[60]. However, in the TIR spectra of the (bi)carbonate region after 5 min (Figure 3.9), no increase in the background absorbance signal of the spectra is observed with increasing DBD power. In our previous work in which *in situ* XAFS was performed under DBD conditions[14], the structure of the catalyst did not change even when the catalyst was charged. In addition, in this study, I set the DBD so as not to directly contact the pellet (Figure 3.2). That is, the effect on the charge of ZnO by DBD in the reaction of CO to ZnO under DBD conditions is excluded. This evidence provides rational support for promoting CO oxidation via the MvK type mechanism by vibrationally-excited CO induced under DBD conditions.

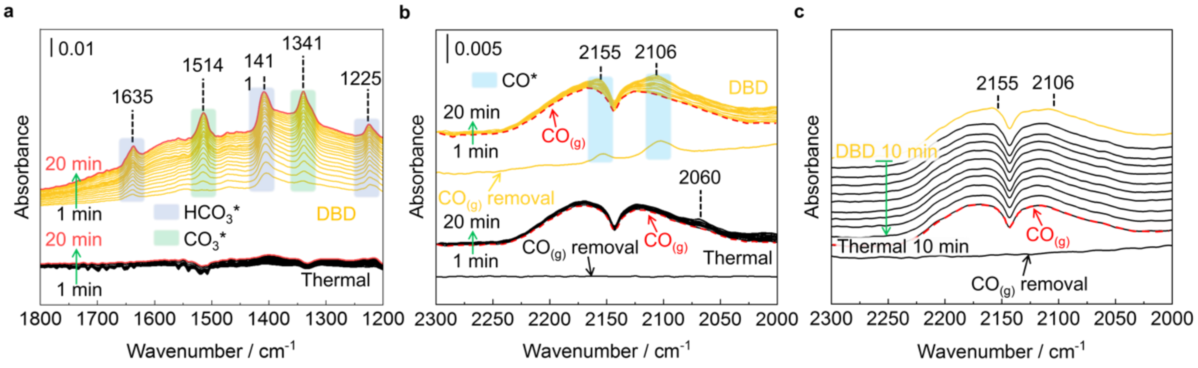

Figure 3.5. *In situ* TIR spectra of (a) (bi)carbonates and (b,c) CO-related region over ZnO under thermal and DBD (0.058 W). ZnO was exposed to 2 % CO in Ar (50 cm^3 min^{-1}) stream at 300 K for 20 min.

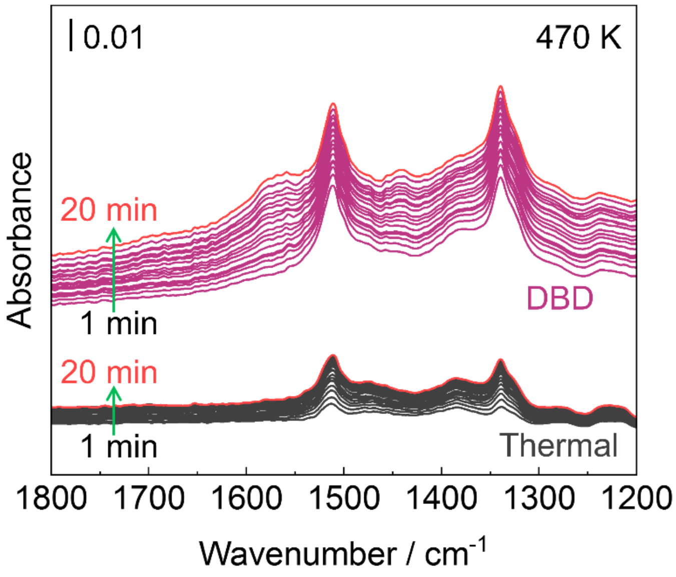

Figure 3.6. *In situ* TIR spectra over ZnO under thermal DBD (0.058 W). The ZnO was pretreated the at 770 K in Ar atmosphere for 1 h, and thereafter exposed to 2 % CO in Ar (50 cm^3 min^{-1}) stream at 470 K for 20 min.

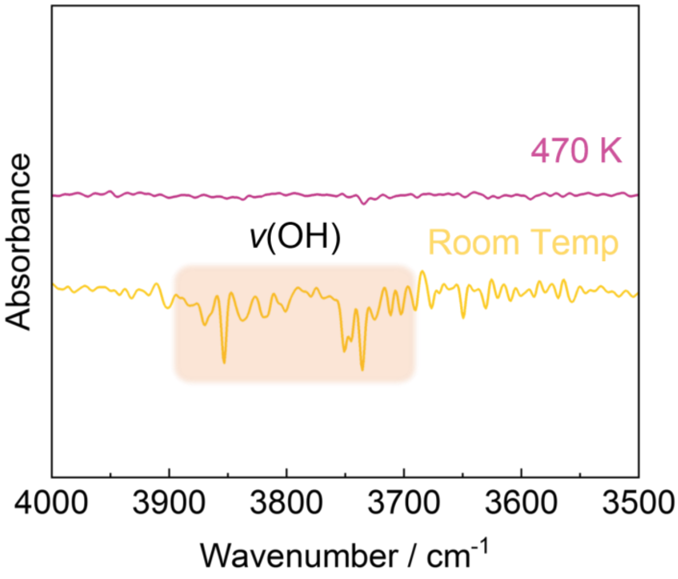

Figure 3.7. *In situ* TIR spectra OH groups region over ZnO under DBD conditions corresponding Figure 3.6 (yellow) and Figure 3.7 (purple).

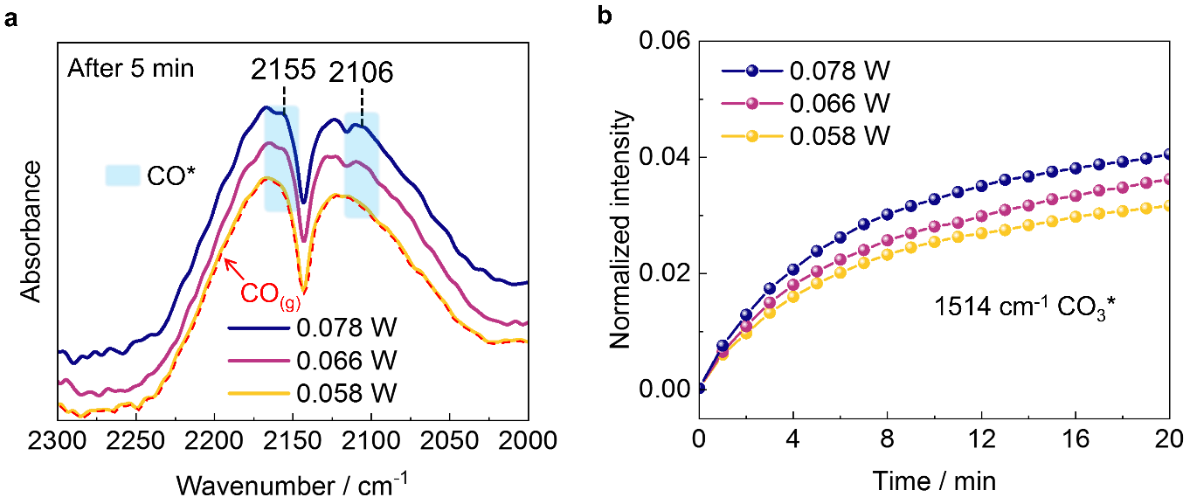

Figure 3.8. (a) *In situ* TIR spectra of CO-related region at different DBD power after 5 min and (b) corresponding evolution of carbonate (1514 cm^{-1}). ZnO was exposed to 2 % CO in Ar (50 cm^3 min^{-1}) stream at 300 K for 20 min with DBD power of 0.058, 0.066, and 0.078 W.

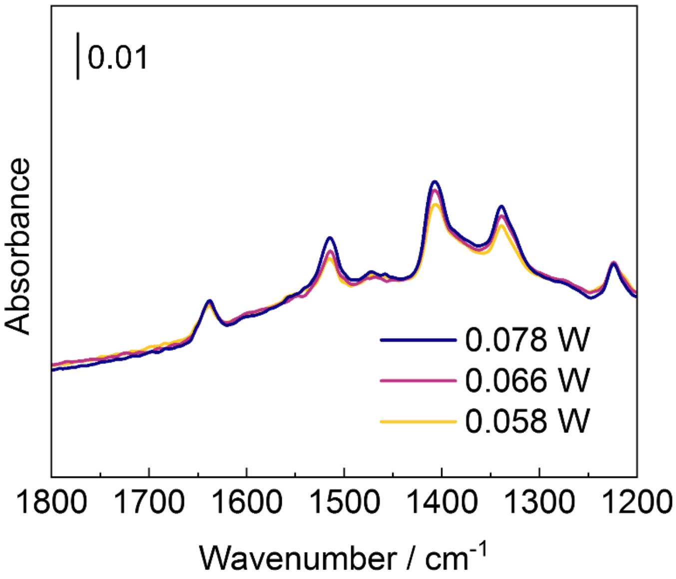

Figure 3.9. *In situ* TIR spectra over ZnO of (bi)carbonate-related region at different DBD power.

3.5 Conclusions

In summary, I were able to unambiguously identify vibrationally-excited CO species with *in situ* TIR diagnostics performed in a catalyst-free environment. The rotational temperature of CO remained unchanged at room temperature at various DBD powers, while the vibrational temperature was increased from 1000 K to 1300 K with DBD power, showing that CO is excited into the vibration quantum number of three. The effect of DBD, or vibrationally-excited CO, was studied using surface reaction over wurtzite ZnO. A comparative study with ground-state CO by *in situ* TIR spectroscopy suggests that vibrationally-excited CO over the ZnO surface promotes thermodynamically limited CO oxidation at room temperature. The spectral evidence shows that vibrationally-excited CO exhibits an unusual CO adsorption band due to strong binding energy with Zn^{2+}, which improves the CO oxidation by activating the reaction with adjacent lattice oxygen in the ZnO via the MvK type mechanism at room temperature (Figure 3.10). The present findings provide new possibilities for achieving low temperature CO oxidation based on the electrification of chemical processes through NTP.

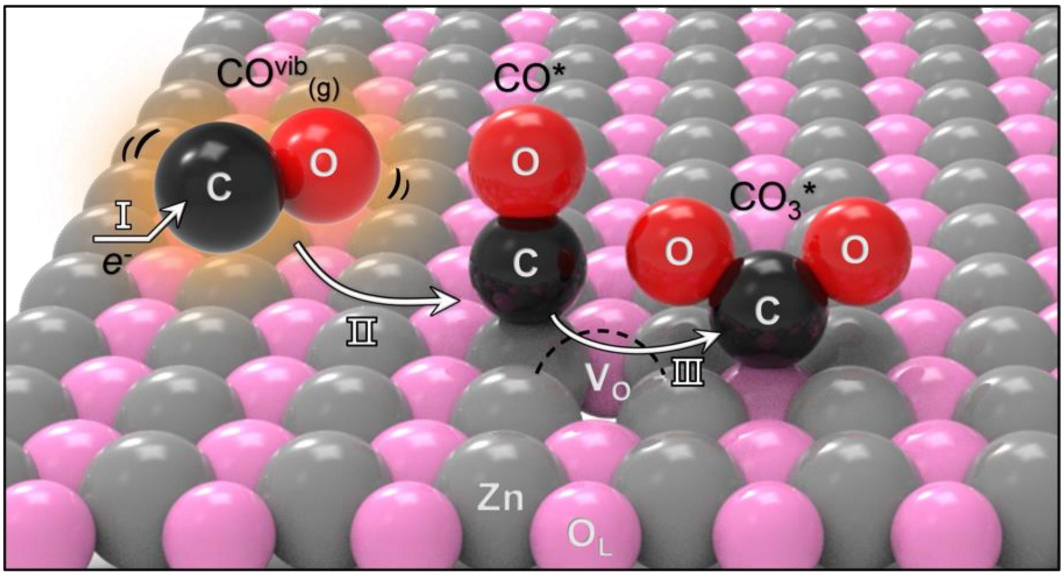

Figure 3.10. Schematic illustration of the promoting CO oxidation via Mars−van Krevelen type mechanism by vibrationally-excited CO over ZnO. V_o: oxygen vacancies, O_L: lattice oxygen. I. Generation of vibrationally-excited CO by electron impact. II. Adsorption of vibrationally-excited CO to Zn^{2+}. III. (Bi)Carbonate formation by reaction with adsorbed CO and adjacent lattice oxygen.

3.6 References

1. X. Chen; Sheng, Z.; Murata, S.; Zen, S.; Kim, H.-H. & Nozaki, T., CH4 dry reforming in fluidized-bed plasma reactor enabling enhanced plasma-catalyst coupling, *J. CO_2 Util.*, **54**, 101771 (2021).
2. A. Bogaerts, et al., The 2020 plasma catalysis roadmap, *J. Phys. D: Appl. Phys.*, **53**, 443001 (2020).
3. A. Bogaerts; Neyts, E. C.; Guaitella, O. & Murphy, A. B., Foundations of plasma catalysis for environmental applications, *Plasma Sources Sci. Technol.*, (2022).
4. Y. Wang; Fan, L.; Xu, H.; Du, X.; Xiao, H.; Qian, J.; Zhu, Y.; Tu, X. & Wang, L., Insight into the Synthesis of Alcohols and Acids in Plasma-driven Conversion of CO2 and CH4 over Copper-based Catalysts, *Appl. Catal. B: Environ*, 121583 (2022).
5. H. Kim, et al., Interim report of plasma catalysis: footprints in the past and blueprints for the future, *Int. J. Plasma Environ. Sci. Technol.*, **15**, e01004 (2021).
6. C. E. Stere, et al., Non-thermal plasma activation of gold-based catalysts for low-temperature water–gas shift catalysis, *Angew. Chem. Int. Ed.*, **56**, 5579-5583 (2017).
7. M. S. AlQahtani; Knecht, S. D.; Wang, X.; Bilén, S. G. & Song, C., One-step low-temperature reduction of sulfur dioxide to elemental sulfur by plasma-enhanced catalysis, *ACS Catal.*, **10**, 5272-5277 (2020).
8. Z. Cui, et al., Plasma-Catalytic Methanol Synthesis from CO2 Hydrogenation over a Supported Cu Cluster Catalyst: Insights into the Reaction Mechanism, *ACS Catal.*, **12**, 1326-1337 (2022).
9. Y. Yi, et al., Selective oxidation of CH4 to CH3OH through plasma catalysis: Insights from catalyst characterization and chemical kinetics modelling, *Appl. Catal. B: Environ*, **296**, 120384 (2021).
10. Y. Wang, et al., Shielding protection by mesoporous catalysts for improving plasma-catalytic ambient ammonia synthesis, *J. Am. Chem. Soc.*, **144**, 12020-12031 (2022).

11. S. Xu; Chen, H.; Hardacre, C. & Fan, X., Non-thermal plasma catalysis for CO2 conversion and catalyst design for the process, *J. Phys. D: Appl. Phys.*, **54**, 233001 (2021).

12. J. C. Whitehead, Plasma–catalysis: the known knowns, the known unknowns and the unknown unknowns, *J. Phys. D: Appl. Phys.*, **49**, 243001 (2016).

13. Y. Sun, et al., Plasma-Catalytic CO2 Hydrogenation over a Pd/ZnO Catalyst: In Situ Probing of Gas-Phase and Surface Reactions, *JACS Au*, **2**, 1800-1810 (2022).

14. D.-Y. Kim, et al., Cooperative Catalysis of Vibrationally Excited CO2 and Alloy Catalyst Breaks the Thermodynamic Equilibrium Limitation, *J. Am. Chem. Soc.*, **144**, 14140-14149 (2022).

15. P. Mehta; Barboun, P.; Herrera, F. A.; Kim, J.; Rumbach, P.; Go, D. B.; Hicks, J. C. & Schneider, W. F., Overcoming ammonia synthesis scaling relations with plasma-enabled catalysis, *Nat. Catal.*, **1**, 269-275 (2018).

16. Z. Sheng; Kim, H.-H.; Yao, S. & Nozaki, T., Plasma-chemical promotion of catalysis for CH 4 dry reforming: unveiling plasma-enabled reaction mechanisms, *Phys. Chem. Chem. Phys.*, **22**, 19349-19358 (2020).

17. Z. Sheng; Watanabe, Y.; Kim, H.-H.; Yao, S. & Nozaki, T., Plasma-enabled mode-selective activation of CH4 for dry reforming: first touch on the kinetic analysis, *Chem. Eng. J.*, **399**, 125751 (2020).

18. E. Neyts & Bogaerts, A., Understanding plasma catalysis through modelling and simulation—a review, *J. Phys. D: Appl. Phys.*, **47**, 224010 (2014).

19. J. Quan, et al., Vibration-driven reaction of CO2 on Cu surfaces via Eley–Rideal-type mechanism, *Nat. Chem.*, **11**, 722-729 (2019).

20. J. Wang; Li, G.; Li, Z.; Tang, C.; Feng, Z.; An, H.; Liu, H.; Liu, T. & Li, C., A highly selective and stable ZnO-ZrO2 solid solution catalyst for CO2 hydrogenation to methanol, *Sci. Adv.*, **3**, e1701290 (2017).

21. C. Wu, et al., Inverse ZrO2/Cu as a highly efficient methanol synthesis catalyst from CO2 hydrogenation, *Nat. Commun.*, **11**, 1-10 (2020).

22. F. Zaera, New advances in the use of infrared absorption spectroscopy for the characterization of heterogeneous catalytic reactions, *Chem. Soc. Rev.*, **43**, 7624-7663 (2014).

23. B. Klarenaar; Engeln, R.; Van Den Bekerom, D.; Van De Sanden, M.; Morillo-Candas, A. & Guaitella, O., Time evolution of vibrational temperatures in a CO2 glow discharge measured with infrared absorption spectroscopy, *Plasma Sources Sci. Technol.*, **26**, 115008 (2017).

24. M. Damen; Martini, L. & Engeln, R., Vibrational quenching by water in a CO2 glow discharge measured using quantum cascade laser absorption spectroscopy, *Plasma Sources Sci. Technol.*, **29**, 095017 (2020).

25. B. Klarenaar; Morillo-Candas, A.-S.; Grofulović, M.; Van De Sanden, M.; Engeln, R. & Guaitella, O., Excitation and relaxation of the asymmetric stretch mode of CO2 in a pulsed glow discharge, *Plasma Sources Sci. Technol.*, **28**, 035011 (2019).

26. S. Xu; Chansai, S.; Xu, S.; Stere, C. E.; Jiao, Y.; Yang, S.; Hardacre, C. & Fan, X., CO Poisoning of Ru Catalysts in CO_2 Hydrogenation under Thermal and Plasma Conditions: A Combined Kinetic and Diffuse Reflectance Infrared Fourier Transform Spectroscopy–Mass Spectrometry Study, *ACS Catal.*, **10**, 12828-12840 (2020).

27. H. Chen, et al., Coupling non-thermal plasma with Ni catalysts supported on BETA zeolite for catalytic CO 2 methanation, *Catal. Sci. Technol.*, **9**, 4135-4145 (2019).

28. H. Chen, et al., CO and H2 activation over g-ZnO layers and w-ZnO (0001), *ACS Catal.*, **9**, 1373-1382 (2018).

29. Z. Zhang, et al., The active sites of Cu–ZnO catalysts for water gas shift and CO hydrogenation reactions, *Nat. Commun.*, **12**, 1-9 (2021).

30. M. Behrens, et al., The active site of methanol synthesis over Cu/ZnO/Al2O3 industrial

catalysts, *Science*, **336**, 893-897 (2012).

31. P. Mars & Van Krevelen, D. W., Oxidations carried out by means of vanadium oxide catalysts, *Chem. Eng. Sci.*, **3**, 41-59 (1954).

32. H. V. Thang & Pacchioni, G., Oxygen vacancy in wurtzite ZnO and metal-supported ZnO/M (111) bilayer films (M= Cu, Ag and Au), *J. Phys. Chem C*, **122**, 20880-20887 (2018).

33. M.-H. Liu; Chen, Y.-W.; Lin, T.-S. & Mou, C.-Y., Defective mesocrystal ZnO-supported gold catalysts: facilitating CO oxidation via vacancy defects in ZnO, *ACS Catal.*, **8**, 6862-6869 (2018).

34. A. Ruiz Puigdollers; Schlexer, P.; Tosoni, S. & Pacchioni, G., Increasing oxide reducibility: the role of metal/oxide interfaces in the formation of oxygen vacancies, *ACS Catal.*, **7**, 6493-6513 (2017).

35. S. Chen; Abdel-Mageed, A. M.; Mochizuki, C.; Ishida, T.; Murayama, T.; Rabeah, J.; Parlinska-Wojtan, M.; Brückner, A. & Behm, R. J. r., Controlling the O-vacancy formation and performance of Au/ZnO catalysts in CO2 reduction to methanol by the ZnO particle size, *ACS Catal.*, **11**, 9022-9033 (2021).

36. H. J. Kim; Jang, M. G.; Shin, D. & Han, J. W., Design of Ceria Catalysts for Low-Temperature CO Oxidation, *ChemCatChem*, **12**, 11-26 (2020).

37. H. Xu; Xu, C.-Q.; Cheng, D. & Li, J., Identification of activity trends for CO oxidation on supported transition-metal single-atom catalysts, *Catal. Sci. Technol.*, **7**, 5860-5871 (2017).

38. E. Pannier & Laux, C. O., RADIS: A nonequilibrium line-by-line radiative code for CO2 and HITRAN-like database species, *J. Quant. Spectrosc. Radiat. Transfer*, **222**, 12-25 (2019).

39. T. Urbanietz; Böke, M.; Schulz-Von Der Gathen, V. & Von Keudell, A., Non-equilibrium excitation of CO2 in an atmospheric pressure helium plasma jet, *J. Phys.*

D: Appl. Phys., **51**, 345202 (2018).

40. C. Stewig; Schüttler, S.; Urbanietz, T.; Böke, M. & Von Keudell, A., Excitation and dissociation of CO2 heavily diluted in noble gas atmospheric pressure plasma, *J. Phys. D: Appl. Phys.*, **53**, 125205 (2020).

41. C. E. Treanor; Rich, J. & Rehm, R., Vibrational relaxation of anharmonic oscillators with exchange-dominated collisions, *J. Chem. Phys.*, **48**, 1798-1807 (1968).

42. A. Fridman, *Plasma chemistry*. Cambridge University Press: Cambridge, 2008.

43. L. Pietanza; Colonna, G. & Capitelli, M., Non-equilibrium plasma kinetics of reacting CO: an improved state to state approach, *Plasma Sources Sci. Technol.*, **26**, 125007 (2017).

44. Z. Zhang; Zhang, L.; Yao, S.; Song, X.; Huang, W.; Hülsey, M. J. & Yan, N., Support-dependent rate-determining step of CO2 hydrogenation to formic acid on metal oxide supported Pd catalysts, *J. Catal.*, **376**, 57-67 (2019).

45. N. C. Nelson; Nguyen, M.-T.; Glezakou, V.-A.; Rousseau, R. & Szanyi, J., Carboxyl intermediate formation via an in situ-generated metastable active site during water-gas shift catalysis, *Nat. Catal.*, **2**, 916-924 (2019).

46. L. Zhang; Zhang, X.; Qian, K.; Li, Z.; Cheng, Y.; Daemen, L. L.; Wu, Z. & Huang, W., Activation and surface reactions of CO and H2 on ZnO powders and nanoplates under CO hydrogenation reaction conditions, *J. Energy Chem.*, **50**, 351-357 (2020).

47. S. Chen; Luo, L.; Jiang, Z. & Huang, W., Size-dependent reaction pathways of low-temperature CO oxidation on Au/CeO2 catalysts, *ACS Catal.*, **5**, 1653-1662 (2015).

48. T. Kropp & Mavrikakis, M., Brønsted–Evans–Polanyi relation for CO oxidation on metal oxides following the Mars–van Krevelen mechanism, *J. Catal.*, **377**, 577-581 (2019).

49. Z. Duan & Henkelman, G., Calculations of CO oxidation over a Au/TiO2 catalyst: a study of active sites, catalyst deactivation, and moisture effects, *ACS Catal.*, **8**, 1376-

1383 (2018).

50. B. Liu; Li, W.; Song, W. & Liu, J., Carbonate-mediated Mars–van Krevelen mechanism for CO oxidation on cobalt-doped ceria catalysts: facet-dependence and coordination-dependence, *Phys. Chem. Chem. Phys.*, **20**, 16045-16059 (2018).

51. B. B. Sarma; Plessow, P. N.; Agostini, G.; Concepción, P.; Pfänder, N.; Kang, L.; Wang, F. R.; Studt, F. & Prieto, G., Metal-specific reactivity in single-atom catalysts: CO oxidation on 4d and 5d transition metals atomically dispersed on MgO, *J. Am. Chem. Soc.*, **142**, 14890-14902 (2020).

52. F.-X. Tian; Zhu, M.; Liu, X.; Tu, W. & Han, Y.-F., Dynamic structure of highly disordered manganese oxide catalysts for low-temperature CO oxidation, *J. Catal.*, **401**, 115-128 (2021).

53. P. R. Shirhatti, et al., Observation of the adsorption and desorption of vibrationally excited molecules on a metal surface, *Nat. Chem.*, **10**, 592-598 (2018).

54. D. Scarano; Spoto, G.; Bordiga, S.; Zecchina, A. & Lamberti, C., Lateral interactions in CO adlayers on prismatic ZnO faces: a FTIR and HRTEM study, *Surf. Sci.*, **276**, 281-298 (1992).

55. D. Scarano; Bertarione, S.; Spoto, G.; Zecchina, A. & Areán, C. O., FTIR spectroscopy of hydrogen, carbon monoxide, and methane adsorbed and co-adsorbed on zinc oxide, *Thin Solid Films*, **400**, 50-55 (2001).

56. V. Schott; Oberhofer, H.; Birkner, A.; Xu, M.; Wang, Y.; Muhler, M.; Reuter, K. & Wöll, C., Chemical activity of thin oxide layers: strong interactions with the support yield a new thin-film phase of ZnO, *Angew. Chem. Int. Ed.*, **52**, 11925-11929 (2013).

57. L. Zhong; Kropp, T.; Baaziz, W.; Ersen, O.; Teschner, D.; Schlögl, R.; Mavrikakis, M. & Zafeiratos, S., Correlation between reactivity and oxidation state of cobalt oxide catalysts for CO preferential oxidation, *ACS Catal.*, **9**, 8325-8336 (2019).

58. H. Noei; Birkner, A.; Merz, K.; Muhler, M. & Wang, Y., Probing the mechanism of low-

temperature CO oxidation on Au/Zno catalysts by vibrational spectroscopy, *J. Phys. Chem C*, **116**, 11181-11188 (2012).

59. Z. Zhang; Fan, L.; Liao, W.; Zhao, F.; Tang, C.; Zhang, J.; Feng, M. & Lu, J.-Q., Structure sensitivity of CuO in CO oxidation over CeO2-CuO/Cu2O catalysts, *J. Catal.*, **405**, 333-345 (2022).

60. H. Noei; Qiu, H.; Wang, Y.; Muhler, M. & Wöll, C., Hydrogen loading of oxide powder particles: A transmission IR study for the case of zinc oxide, *ChemPhysChem*, **11**, 3604-3607 (2010).

Chapter 4. Summary and future work

4.1 Summary

In this thesis, I focused on elucidating the reaction mechanism of NTP-assisted catalysis, especially the interplay between vibrationally-excited molecules (e.g. CO_2^{vib} and CO^{vib}) and catalytic surfaces. The content includes (i) surface reaction of vibrationally-excited CO_2 and alloy catalysts via the E−R type mechanisms, and (ⅱ) probing of vibrationally-excited CO-induced MvK type mechanisms over reducible catalysts.

In the first part, I presented that compared with the conventional thermal catalysis, the NTP-assisted Pd_2Ga/SiO_2 alloy catalysis improve CO_2 hydrogenation. It is worth highlighting that the combination of alloy catalyst and NTP could be beyond the thermodynamic limitation that is impossible to achieve with conventional thermal catalysis. Upon the agreement of approaches coupling experimental−theoretical study, the bending mode of vibrationally-excited CO_2 could lower the energy barrier and react with hydrogen atoms adsorbed on Pd sites via the E−R type mechanisms and then accelerate formate formation due to the oxyphilic nature of neighboring Ga site. The results demonstrated the reaction mechanism of fast formation and decomposition of monodentate formate, not only CO_2 activation but also H_2 activation is expected. In addition, the *in situ* XAFS results confirmed that a structural change of the alloy catalyst and NTP heating affecting the CO_2 hydrogenation are fully ruled out. I believed that the present study enables the high designability of CO_2 hydrogenation catalysts toward value-added chemicals based on electrification via NTP.

In the second part, I investigated CO in DBD by applying *in situ* TIR diagnostics and identified vibrationally-excited CO with a catalyst-free environment. The rotational temperature of CO remained at room temperature (ca. 300 K) with various DBD power, while the vibration temperature increased from 1000 K to 1300 K. The density of the vibrational excitation levels was predicted under the assumption that the vibrational energies followed the

Boltzmann distribution, indicating the density of the vibrationally-excited CO was controlled by the DBD power and the population distribution of vibrationally-excited CO up to a quantum number of three. These insights allowed the quantitatively identification of the surface reaction channels of vibrationally-excited CO. Subsequently I carefully examined the effect of DBD or vibrationally-excited CO on the surface reaction on wurtzite ZnO. From the comparative studies through with ground-state CO suggest that vibrationally-excited CO over the surface of wurtzite ZnO promotes thermodynamically limited CO oxidation. More precisely, ZnO remains inert with ground-state CO, whereas vibrationally-excited CO exhibits an unusual CO adsorption band due to strong binding energy with Zn^{2+}, which promotes the CO oxidation by activating the reaction with adjacent lattice oxygen via the MvK type mechanism. These findings show that new pathway for achieving low temperature based on the electrification of via NTP. Furthermore, in addition to the L−H and E−R type mechanisms, the findings support the utility of MvK type mechanism, which is one of the three basic catalytic surface reaction mechanisms of vibrationally-excited molecules in NTP-assisted catalysis.

4.2 Future work

In the long-term low carbon strategies announced by major countries around the world, CO_2 capture, and utilization technology was included as a key strategic tool. Meanwhile, as renewable energy spreads, the demand for chemical conversion using electric power increases[1,2], low-carbon technology related to electrification of chemical process such as NTP or Power-to-Gas are attracting attention in the environment and energy fields[3-7]. In particular, as a long-term strategy for carbon recycling, fundamental study using nonthermal plasma is being actively conducted in China and Europe[5,8-16]. However, most of the studies are dominated by the chemical conversion of CO_2, so study on mineralization or utilization as an energy material is relatively weak.

As a future plan, the content includes CO_2 (i) chemical conversion, (ii) energy conversion, and (iii) mineralization.

In the first part, adopting the nonthermal plasma assisted catalysis conducted in the doctoral course, accelerates the study of using CO_2 as a reactant and converting it into various carbon compounds such as fuels and basic chemicals through chemical conversion. In more detail, I plan to conduct a study focusing on the promotion of catalysis through the Langmuir−Hinshelwood type mechanism of vibrationally-excited CO_2, which is not covered in this thesis. Furthermore, I explore the effect of nonthermal plasma activated H_2 on the reaction in depth.

The second part is the conversion of CO_2 as an energy material. Carbon black is used as black pigments, as a reinforcing filler in tires and in a variety of rubber applications[17]. Carbon black also has high electrical conductivity, and the porosity and surface chemistry can be altered to achieve the properties that best suit the application[18]. These properties can be very suitable for renewable energy applications. Therefore, I plan to conduct research on synthesizing carbon black from CO_2 via NTP and applying it as an anode material or conductive additive for Li, Na and K ion batteries.

Finally, the third part is CO_2 mineralization. CO_2 mineralization is the storage process of CO_2 in the form of water insoluble Ca/$MgCO_3$. In particular, CO_2 mineralization by alkaline solid waste is a promising option for climate change mitigation in countries with enormous amounts of waste[19]. Alkaline ash, a byproduct of fuel combustion in thermal power plants, such as coal fly ash and municipal solid waste incineration ash, is a promising feedstock for CO_2 mineralization due to its high alkalinity and abundance[20,21]. In addition, with the additional utilization of carbonate ash as a construction material, CO_2 mineralization can be integrated with the utilization of carbonate ash in the manufacture of building materials to achieve a waste-to-resource supply chain[22]. However, the biggest obstacle to the large-scale application of CO_2 mineralization is the slow. The key steps involved in CO_2 mineralization are energy intensity[23]. Thus, the energy demand for CO_2 mineralization may offset potential greenhouse gas emission reductions. In this thesis, I presented that thermodynamically limited reactions can be improved by NTP. From these insights, the application of NTP can be a promising solution to achieve CO_2 removal efficiencies for the slow kinetics of CO_2 mineralization. Therefore, I investigate the screening of optimal alkaline ashes in NTP and the utilization of products of NTP-assisted mineralization in the production of construction materials.

4.3 References

1. J. DeAngelo; Azevedo, I.; Bistline, J.; Clarke, L.; Luderer, G.; Byers, E. & Davis, S. J., Energy systems in scenarios at net-zero CO2 emissions, *Nat. Commun.*, **12**, 1-10 (2021).
2. D. Gielen, et al., World energy transitions outlook: 1.5° C pathway, (2021).
3. A. Bogaerts, et al., The 2020 plasma catalysis roadmap, *J. Phys. D: Appl. Phys.*, **53**, 443001 (2020).
4. J. C. Whitehead, Plasma–catalysis: the known knowns, the known unknowns and the unknown unknowns, *J. Phys. D: Appl. Phys.*, **49**, 243001 (2016).
5. A. George; Shen, B.; Craven, M.; Wang, Y.; Kang, D.; Wu, C. & Tu, X., A Review of Non-Thermal Plasma Technology: A novel solution for CO2 conversion and utilization, *Renew. Sust. Energy Rev.*, **135**, 109702 (2021).
6. A. Bogaerts; Neyts, E. C.; Guaitella, O. & Murphy, A. B., Foundations of plasma catalysis for environmental applications, *Plasma Sources Sci. Technol.*, (2022).
7. I. Adamovich, et al., The 2022 Plasma Roadmap: low temperature plasma science and technology, *J. Phys. D: Appl. Phys.*, **55**, 373001 (2022).
8. M. Damen; Martini, L. & Engeln, R., Vibrational quenching by water in a CO2 glow discharge measured using quantum cascade laser absorption spectroscopy, *Plasma Sources Sci. Technol.*, **29**, 095017 (2020).
9. B. Klarenaar; Engeln, R.; Van Den Bekerom, D.; Van De Sanden, M.; Morillo-Candas, A. & Guaitella, O., Time evolution of vibrational temperatures in a CO2 glow discharge measured with infrared absorption spectroscopy, *Plasma Sources Sci. Technol.*, **26**, 115008 (2017).
10. B. Klarenaar; Morillo-Candas, A.-S.; Grofulović, M.; Van De Sanden, M.; Engeln, R. & Guaitella, O., Excitation and relaxation of the asymmetric stretch mode of CO2 in a pulsed glow discharge, *Plasma Sources Sci. Technol.*, **28**, 035011 (2019).
11. Z. Cui, et al., Plasma-Catalytic Methanol Synthesis from CO2 Hydrogenation over a

Supported Cu Cluster Catalyst: Insights into the Reaction Mechanism, *ACS Catal.*, **12**, 1326-1337 (2022).

12. S. Xu; Chansai, S.; Xu, S.; Stere, C. E.; Jiao, Y.; Yang, S.; Hardacre, C. & Fan, X., CO Poisoning of Ru Catalysts in CO_2 Hydrogenation under Thermal and Plasma Conditions: A Combined Kinetic and Diffuse Reflectance Infrared Fourier Transform Spectroscopy–Mass Spectrometry Study, *ACS Catal.*, **10**, 12828-12840 (2020).
13. L. Wang; Yi, Y.; Guo, H. & Tu, X., Atmospheric pressure and room temperature synthesis of methanol through plasma-catalytic hydrogenation of CO2, *ACS Catal.*, **8**, 90-100 (2018).
14. S. Xu, et al., Mechanistic study of non-thermal plasma assisted CO_2 hydrogenation over Ru supported on MgAl layered double hydroxide, *Appl. Catal. B: Environ*, **268**, 118752 (2020).
15. S. Xu; Chen, H.; Hardacre, C. & Fan, X., Non-thermal plasma catalysis for CO2 conversion and catalyst design for the process, *J. Phys. D: Appl. Phys.*, **54**, 233001 (2021).
16. Y. Sun, et al., Plasma-Catalytic CO2 Hydrogenation over a Pd/ZnO Catalyst: In Situ Probing of Gas-Phase and Surface Reactions, *JACS Au*, **2**, 1800-1810 (2022).
17. K.-H. Nam; Chae, K. H.; Choi, J.-H.; Jeon, K.-J. & Park, C.-M., Superior carbon black: High-performance anode and conducting additive for rechargeable Li-and Na-ion batteries, *Chem. Eng. J.*, **417**, 129242 (2021).
18. S. Khodabakhshi; Fulvio, P. F. & Andreoli, E., Carbon black reborn: Structure and chemistry for renewable energy harnessing, *Carbon*, **162**, 604-649 (2020).
19. D. B. Viet; Chan, W.-P.; Phua, Z.-H.; Ebrahimi, A.; Abbas, A. & Lisak, G., The use of fly ashes from waste-to-energy processes as mineral CO2 sequesters and supplementary cementitious materials, *J. Hazard. Mater.*, **398**, 122906 (2020).
20. L. Ji; Zheng, X.; Zhang, L.; Feng, L.; Li, K.; Yu, H. & Yan, S., Feasibility and

mechanism of an amine-looping process for efficient CO2 mineralization using alkaline ashes, *Chem. Eng. J.*, **430**, 133118 (2022).

21. A. Dindi; Quang, D. V.; Vega, L. F.; Nashef, E. & Abu-Zahra, M. R., Applications of fly ash for CO2 capture, utilization, and storage, *J. CO_2 Util.*, **29**, 82-102 (2019).

22. S.-Y. Pan; Chen, Y.-H.; Fan, L.-S.; Kim, H.; Gao, X.; Ling, T.-C.; Chiang, P.-C.; Pei, S.-L. & Gu, G., CO2 mineralization and utilization by alkaline solid wastes for potential carbon reduction, *Nat. Sustain.*, **3**, 399-405 (2020).

23. H. Ostovari; Müller, L.; Skocek, J. & Bardow, A., From unavoidable CO2 source to CO2 sink? A cement industry based on CO2 mineralization, *Environ. Sci.Technol.*, **55**, 5212-5223 (2021).

Acknowledgements

膨らんだ夢を抱いて東京で始めた留学生活は、私の人生で忘れられない大切な時間になりました。私には長いようで短い期間でしたが、とても充実した日々を送ることができました。博士号を取得する為に努力し、結果として学位課程を終えることができました。私がこの博士課程を無事に終えるまで、私の努力だけがすべてではなかったと思います。私のそばで力になってくれた大切な方々、新しく縁を結んで苦楽を共にした方々にこの文書を通じて感謝の気持ちをお伝えしたいと思います。

在学中、私を指導して下さった野崎先生に感謝の言葉を申し上げます。いつも熱意のある指導と応援のおかげで私を挑戦的な研究者に成長させて頂きました。尊敬する先生の下で、研究者としての能力だけでなく多くのことを学ぶことができ、感謝の気持ちでいっぱいです。先生が教えて下さった「何事にも挑戦する姿勢」と「研究に対する情熱」は、私の留学生活にとても良い影響となりました。そのような先生の考え方と情熱を忘れずに将来自分もそのような姿になるよう努力し、常に最善を尽くしたいと思います。そして、今まで以上に先生と研究について深く共有できる関係でありたいです。

お忙しい中、私の論文審査に参加してくださった関口先生、山中先生、山本先生、笹部先生に深く感謝の言葉を申し上げます。 先生方の助言をもとに、しっかりとした研究者に成長していきます。

プラズマと触媒分野に多くのことを教えてくださったAISTの金賢夏先生、北海道大学の佐々木先生、高草木先生、古川先生に感謝の言葉を申し上げます。

いつも私を応援してくださり、全面的に支援してくださった修士課程の指導教授のカン先生、ありがとうございます。

野崎研という一つのグループで縁を結んで過ごしたメンバーにも感謝の言葉をお伝えしたいと思います。私たちのメンバーと一緒に過ごした時間は私にはとても大切でした。いつも熱心で善良なメンバーといい絆を結ぶことができたのも留学生活の間、もらった大切なプレゼントだと思っております。恥ずかしがり屋で言葉で表現は

出来ませんでしたが、今まで研究室に来る度にいつも明るい笑顔で喜んで迎えてくれて本当にありがとうございました。

新たな研究分野に参入した為、自分の方向と意味を掴むために悩みながら大変だった東京生活の初めごろから、生活に慣れるまでたくさん助けて頂いた齋藤さん、Zunrong さん、武塙さん、皆様が目標に至る事を心から応援しています。

近くで面倒を見てくれたり、私のお願いには情熱と誠意を尽くして自分の事のように助けてくれた同期の Chen、円満な性格でみんなと仲が良い同期の Chunyan、研究室に慣れるように助けてくれたり、実験にも助けて頂きありがとうございます。どこへ行ってもどんな研究をしてもうまくやっていくと信じています。

野崎先生の 1 号女性弟子 Xu さん、Xu さんが私の在学中にどれだけ大きな支えになったか分かりません。修士の卒業おめでとうございます。社会人として Xu さんの未来を応援します。

そして同じ時期に日本に留学することになった Husein、遅くなりましたが、結婚おめでとうございます。そして、素敵な家庭を築いて、また研究者として成長して行くことを望みます。2021 年冬、Xu さんと一緒にクラシック公演も見て写真も撮ったその大切な記憶を残してくれてありがとうございます。

北京工科大学から 1 年間訪問教授として来られた Fan 先生、先生の新しいことへの挑戦と研究に対する情熱を同じ研究室で見ることができ、たくさんの経験をする事が出来ました。東京にいらっしゃる間、良い思い出をたくさん作れることを祈ります。

研究室で私の話し相手になってくれたジファン君、井関さん、牧野さん、中島さんに感謝の気持ちを伝えます。話を交わすだけで私に大きな力になってくれました。これから社会人として経験する難関を賢明に克服することを願います。

研究室の後輩 Li、Wenjun、河端さん、杉永さん、学会に参加したりディフェンスの準備したり、たくさんの会話ができなくて残念でした。研究の面でも、人間的な面でもお手本になるような先輩になりたかったのに、あまり立派な姿を見せられなくてごめんなさい。これから残った在学期間を素敵に終えることを祈ります。

修士の時から一緒に日本への留学を選択した大阪大学のボムドクさん、ヒョジンさんや名古屋大学のギドンさん、修士の頃、初めて会食の時に会って挨拶したのが昨日のようですが、いつのまにか5年という時間が経ちました。10年後も20年後も今のようにお互いに慰めと励ましになってくれる仲になりましょう。

在学中、研究に邁進できるよう心強く応援してくださった両親に心より感謝を申し上げます。これからはその心に報いる息子になります。

実は卒業だと思った頃から最後の文章を頭の中でいつも描いていました。無数の文章が擦れて、整えて消して、書いてを繰り返しましたが、いざディフェンスを終えたら心が淡々としました。私がここに住んでいて、この文章を書くことができ、念願の博士号を取ることができるという事実に、私はただ感謝するだけです。感謝しているという言葉以外にはこれ以上表現する方法がないと思います。新たなスタートと共に、さらに頑張ります。

2023年2月